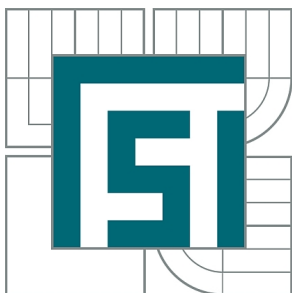


VYSOKÉ UČENÍ TECHNICKÉ V BRNĚ
BRNO UNIVERSITY OF TECHNOLOGY



FAKULTA STROJNÍHO INŽENÝRSTVÍ
ÚSTAV FYZIKÁLNÍHO INŽENÝRSTVÍ
FACULTY OF MECHANICAL ENGINEERING
INSTITUTE OF PHYSICAL ENGINEERING

PREPARATION AND UTILIZATION OF EXFOLIATED GRAPHITE/GRAPHENE LAYERS IN NANOSENSORICS

PŘÍPRAVA A POUŽITÍ EXFOLIOVANÝCH GRAFITOVÝCH/GRAFENOVÝCH VRSTEV V OBLASTI
NANOSENZORIKY

DIPLOMOVÁ PRÁCE
MASTER'S THESIS

AUTOR PRÁCE
AUTHOR

Bc. MILOŠ HRABOVSKÝ

VEDOUCÍ PRÁCE
SUPERVISOR

Ing. MIROSLAV BARTOŠÍK, Ph.D.

BRNO 2014

Vysoké učení technické v Brně, Fakulta strojního inženýrství

Ústav fyzikálního inženýrství

Akademický rok: 2013/2014

ZADÁNÍ DIPLOMOVÉ PRÁCE

student(ka): Bc. Miloš Hrabovský

který/která studuje v **magisterském navazujícím studijním programu**

obor: **Fyzikální inženýrství a nanotechnologie (3901T043)**

Ředitel ústavu Vám v souladu se zákonem č.111/1998 o vysokých školách a se Studijním a zkušebním řádem VUT v Brně určuje následující téma diplomové práce:

Příprava a použití exfoliovaných grafitových/grafenových vrstev v oblasti nanosenzoriky

v anglickém jazyce:

Preparation and Utilization of Exfoliated Graphite/Graphene Layers in Nanosensorics

Stručná charakteristika problematiky úkolu:

Grafénová vrstva vykazuje značnou závislost svých transportních vlastností na přítomnosti už jednotlivých molekul plynu. Z tohoto důvodu je grafén předurčen pro aplikace v oblasti senzorů. Cílem této práce je navrhnout, vyrobit (pomocí EBL) vhodné nanostruktury na exfoliovaném grafénu a testovat odezvu takto připravených nanostruktur na změny relativní vlhkosti (případně koncentrace jiných plynů N₂, Ar).

Cíle diplomové práce:

1. Vypracujte literární rešerši uvedené problematiky.
2. Navrhněte vhodné nanostruktury umožňující dvoubodové, případně čtyřbodové měření odezvy transportních vlastností (vhodné pro účely nanosenzoriky).
3. Pomocí EBL připravte navržené nanostruktury, buď vhodným rozmístěním elektrických kontaktů, nebo tvarováním vrstvy exfoliovaného grafénu.
4. Proved'te měření závislosti změn transportních vlastností na změně relativní vlhkosti a porovnejte jednotlivé typy nanosenzorů z hlediska jejich citlivosti.

Seznam odborné literatury:

- [1] DAN, Yaping, Ye LU, Nicholas J. KYBERT, Zhengtang LUO a A. T. Charlie JOHNSON. Intrinsic Response of Graphene Vapor Sensors. Nano Letters. 2009-04-08, vol. 9, issue 4, s. 1472-1475.
- [2] SCHEDIN, F., et al.: Detection of individual gas molecules adsorbed on graphene. Nature Materials, Vol. 9, 2007, p. 652-655. ISSN 1476-1122
- [3] KO, G., H.-Y. KIM, J. AHN, Y.-M. PARK, K.-Y. LEE a J. KIM. Graphene-based nitrogen dioxide gas sensors. Current Applied Physics. 2010, vol. 10, issue 4, s. 1002-1004.

Vedoucí diplomové práce: Ing. Miroslav Bartošík, Ph.D.

Termín odevzdání diplomové práce je stanoven časovým plánem akademického roku 2013/2014.

V Brně, dne 12.12.2013

L.S.

prof. RNDr. Tomáš Šíkola, CSc.
Ředitel ústavu

prof. RNDr. Miroslav Doupovec, CSc., dr. h. c.
Děkan fakulty

BRNO UNIVERSITY OF TECHNOLOGY

Preparation and Utilization of Exfoliated Graphite/Graphene Layers in Nanosensorics

Author: Miloš Hrabovský

Supervisor: Miroslav Bartošík

Faculty of Mechanical Engineering

Institute of Physical Engineering

2013/2014

Declaration of Authorship

I, Miloš Hrabovský, declare that this thesis titled, ‘Preparation and Utilization of Exfoliated Graphite/Graphene Layers in Nanosensorics’ and the work presented in it are my own. I confirm that:

- This work was done wholly or mainly while in candidature for a research degree at this University.
- Where any part of this thesis has previously been submitted for a degree or any other qualification at this University or any other institution, this has been clearly stated.
- Where I have consulted the published work of others, this is always clearly attributed.
- Where I have quoted from the work of others, the source is always given. With the exception of such quotations, this thesis is entirely my own work.
- I have acknowledged all main sources of help.
- Where the thesis is based on work done by myself jointly with others, I have made clear exactly what was done by others and what I have contributed myself.

Signed:

Date:

Abstrakt

Tato diplomová práce se věnuje výrobě vrstev grafitu/grafenu a měření jejich transportních vlastností v závislosti na relativní vlhkosti. Grafenové šupinky byly nanášeny pomocí mechanického odlupování. Pro kontaktování grafenových šupinek byla využita elektronová litografie a na pozorování byly využity optická mikroskopie, mikroskopie atomárních sil a elektronová mikroskopie. V práci jsou popsány jednotlivé kroky výroby, analýzy a měření transportních vlastností nanesených grafenových šupinek.

Abstract

This diploma thesis deals with the fabrication of graphite/graphene layers and measurement of their transport properties as a function of relative humidity. Graphene flakes were deposited by mechanical exfoliation. For contacting the graphene flakes the electron beam lithography was used. Additional characterization was performed by optical microscopy, atomic force microscopy and scanning electron microscopy. The thesis describes the steps for the production, observation and characterization of the deposited graphene flakes.

Klíčová slova

grafen, AFM, EBL, SEM, grafit, litografie, čtyřbodová metoda, V–A měření

Keywords

graphene, AFM, EBL, SEM, graphite, lithography, four point probe method, V–A measurement

Acknowledgements

Foremost, I would like to express my sincere gratitude to my supervisor Ing. Miroslav Bartošík for the continuous support during my studies and research, for his patience, motivation, enthusiasm, and immense knowledge. His guidance helped me in all the time of research and writing of this thesis. My sincere thanks also goes to Ing. Pavel Procházka and Bc. Jan Hulva for helping me with the transport measurements. Also I would like to thank Ing. Zuzana Lišková for helping me with the electron beam lithography. Last but not the least, I would like to thank my family: my parents for supporting me spiritually throughout my life.

Contents

Declaration of Authorship	iii
Abstract	v
Acknowledgements	vii
1 Introduction	1
2 Graphene–based nanosensors	3
2.1 Preparation and utilization	3
2.1.1 CVD graphene	3
2.1.2 Micromechanical cleavage of graphite	4
2.1.3 Reduced graphene oxide	4
2.1.4 Epitaxially grown graphene	4
2.1.5 Localization and analysis	5
2.2 Nanosensor types	6
2.2.1 Resistive graphene–based nanosensor	7
2.2.2 Field effect transistor (FET) nanosensor	7
2.2.3 Surface acoustic wave (SAW) nanosensor	8
2.2.4 Quartz crystal microbalance (QCM) nanosensor	8
2.2.5 Micro electromechanical systems (MEMS) nanosensor	9
2.2.6 Metal oxide hybrid nanosensor	10
2.3 Graphene–based sensor fabrication methods	10
2.4 Detection of Gas molecules	11
2.4.1 NO ₂ detection	12
2.4.2 H ₂ O detection	13
2.4.3 CO ₂ detection	14
2.4.4 Impurities	16
2.5 Doping of graphene	17
3 Experimental setup	21
3.1 Design of structures for transport measurement	21

3.1.1	2–point probe structures	21
3.1.2	4–point probe structures	22
3.1.3	Sample holder	23
3.2	Fabrication of structures for transport measurement	23
3.2.1	Spincoating of PMMA	24
3.2.2	Electron beam lithography	25
3.2.3	Development of the exposed structures	32
3.2.4	Ion beam deposition	32
3.2.5	Lift–off process	33
3.2.6	Summary of the metallic contacts fabrication	33
3.3	Graphene exfoliation	33
3.4	Atomic force microscopy	34
3.5	Raman spectroscopy	36
3.5.1	Raman spectroscopy of graphene	38
4	Experimental setup 2	41
4.1	Transport measurement	41
4.1.1	2–point probe measurement	41
4.1.2	4–point probe measurement	42
4.2	Setup of the transport properties measurement as a function of relative humidity	43
5	Results	47
5.1	2–point probe measurement of the graphene sensor response	47
5.1.1	Finger like electrodes	47
5.1.2	Universal electrodes	49
5.1.3	Graphene flake with universal electrodes by applying a gate voltage	50
5.1.4	Electric field effect measurement of the graphene sensor . . .	53
5.2	KPFM measurement of the graphene sensor	54
5.2.1	Using a lock–in amplifier	54
5.2.2	Using a constant current source	57
6	Conclusion	59
	Bibliography	61

Chapter 1

Introduction

The ultimate goal of nanosensors is the ability to detect individual quanta of a measured value. In case of sensing gas and chemical vapors, the quantum is one molecule. The limiting factors of current sensors are the fluctuations due to thermal motion of charge carriers and defects because the intrinsic noise exceeds the signal from individual target molecules by an order of magnitude [1]. Additionally since conventional sensors are three dimensional (3D), the change of conductivity of the topmost layer after adsorption of the target molecule does not affect the overall conductivity enough to detect it. Currently, the highest resolution of all nanosensors was reported using carbon nanotube-based (CNT) and graphene-based sensors.

Graphene, a single layer of sp^2 hybridized carbon atoms arranged in a honeycomb lattice, was prepared by Geim and Novoselov in 2004 [2]. Unlike charge carriers in traditional semiconductor materials, electrons and holes in graphene have linear energy dispersion relation; their behavior is similar to massless particles, so-called Dirac fermions. This unique electrical property, and the fact that graphene is transparent, conducting, bendable and is one of the strongest materials known, makes it a promising material for future electronic applications like nanosensors.

Graphene-based nanosensors are capable of detecting individual molecules attaching (adsorbing) or detaching (desorbing) from the surface. The extraordinary sensitivity was promoted by Prof. Andre Geim: "Graphene has the ultimate sensitivity because in principle it cannot be beaten—you cannot get more sensitive than a single molecule [3]. Since every atom of the graphene layer is a surface atom,

with the possibility of interacting with one molecule of the target gas or chemical vapor, graphene has an ultrasensitive sensor response, which should allow for high detection range; from a single molecule to a high concentration of target molecules. The adsorption and desorption of molecules changes the free electron concentration (increases or decreases depending if the target molecule behaves like a donor or an acceptor), which leads to a change in electrical conductivity of the graphene-based nanosensor. Through this change of conductivity we detect the concentration of adsorbed molecules.

Since pristine graphene has no specific functionalization to detect only one kind of molecule, the surface needs to be functionalized by polymers or metals to enhance specific molecule detection. Thin film of a functionalizing material creates trapping centers for target molecules; the adsorption at such location changes the local conductivity of the measured sensor. Different types of nanosensors based on using a single layer or a multilayer graphene are used for gas and chemical vapor measurements. Most common configurations are resistive sensors [1], field effect transistors (FET) [4], the surface acoustic wave (SAW) [5], the quartz crystal microbalance (QCM) [6], micro electrochemical systems (MEMS) [7], and metal oxide hybrid sensors [8].

Graphene in nanosensors is produced using a CVD method, micromechanical and chemical exfoliation of graphite, reduction of graphene-oxide and epitaxial growth.

In this thesis, the measurement of transport properties of an exfoliated graphene sensor as a function of relative humidity will be studied. The review of the current state of graphene-based nanosensors can be found in Chapter 2. Fabrication and characterization is mentioned in Chapter 3, the setup for transport properties measurement is in Chapter 4 and the results can be found in Chapter 5.

Chapter 2

Graphene–based nanosensors

2.1 Preparation and utilization

First graphene was prepared using micromechanical exfoliation by Novoselov and Geim in 2004 [9]. Since then a lot of effort has been spent to develop faster and more efficient ways of graphene production on small and large area scale.

2.1.1 CVD graphene

Chemical vapor deposition (CVD) of a single or multilayered graphene is a very popular method for nanosensing applications. The fabrication procedure is performed in a vacuum furnace using either crystal quartz plates [10] or a polycrystalline copper foil (99.999%) [11]. The foil is heated up to 800-1200 °C annealed in Ar/H₂ [11] for 30 minutes and then pure CH₄ or a mixture of CH₄ and Ar is used to grow the graphene on top of the substrate. The top side of the copper foil is usually covered with PMMA and the copper foil is etched away in FeCl₃ solution. After the etching is complete, graphene with PMMA is washed in deionized water and transferred to the surface of thermally oxidized Si substrates [11].

2.1.2 Micromechanical cleavage of graphite

Graphite consists of many stacked layers of graphene bonded together by weak van der Waals force. By exfoliation (cleavage) using mechanical or chemical energy, it is possible to break these bonds and prepare a pristine layer of graphene.

The graphene is prepared by two methods: the standard mechanical exfoliation of a highly ordered pyrolytic graphite (HOPG) using a low adhesion scotch tape [1, 12–15], or by stamping method using PDMS stamps on HOPG dry etched in oxygen plasma, so that the graphene flakes could be transferred to a specific place on the surface of thermally oxidized Si substrates [16] with a considerably less amount of residue left on the surface than when using the scotch tape method.

2.1.3 Reduced graphene oxide

Formerly known as graphitic oxide or graphitic acid, it consists of carbon, oxygen and hydrogen in different ratios. Graphene oxide is obtained by treating graphite using strong oxidizers. As an example, graphite may be reacted with sulfuric acid, nitric acid and potassium chlorate for 96 hours. After the oxidation it is washed with a HCl solution and with deionized water to neutralize the solution. The neutral solution is poured on the surface of thermally oxidized Si substrate and then the thermal reduction forms the final reduced graphene oxide [17, 18].

2.1.4 Epitaxially grown graphene

Epitaxial graphene has attracted a lot of attention by the semiconductor industry due to post-CMOS (Complementary Metal Oxide Semiconductor) technology applications. Epitaxial growth of graphene requires epitaxially prepared surface like SiC or Si substrate and consists of 2 steps. The first step, a 3C-SiC thin film is formed on the silicon substrate by using a molecular-beam epitaxy (MBE), is followed by the second step: graphitization. The SiC thin film is annealed in a vacuum at $\approx 2000^\circ\text{C}$ [19]. This method produces between 1 and 3 layers of graphene. The height depends on the decomposition temperature.

2.1.5 Localization and analysis

Graphene flakes and layers can be observed and analysed using different observation techniques such as: optical microscopy [1, 13, 16], electron microscopy (SEM, TEM) [11, 15–18], atomic force microscopy (AFM) [10, 14–16, 19] and Raman spectroscopy [10, 11].

Figure 2.1 shows an optical image of a graphene flake on top of thermally oxidized Si substrate without any modification of the graphene shape. Figure 2.2 shows a graphene flake modified using plasma etching to pattern the Hall bar geometry.

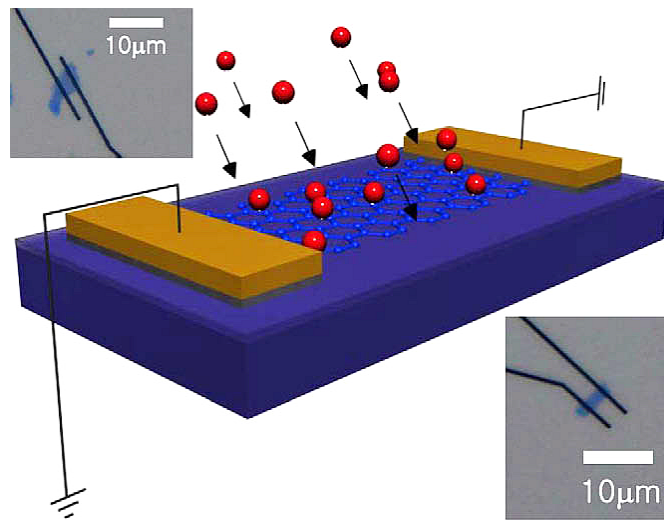


FIGURE 2.1: Schematic diagram of a sensor based on exfoliated graphene (Insets are pictures of the real structure imaged by an optical microscope) [13].

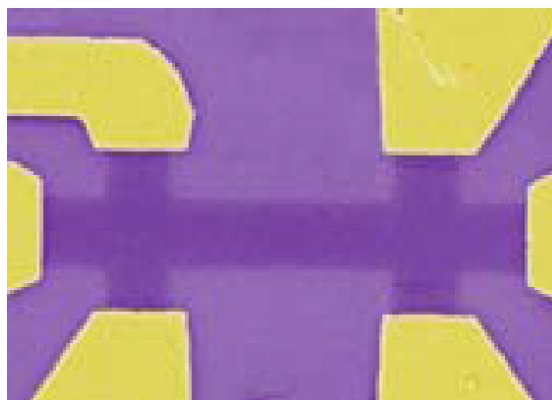


FIGURE 2.2: Optical image of a graphene flake modified to a Hall bar shape [1].

Images obtained by TEM (Fig 2.3A) show a wrinkled graphene sheet with no aggregation, the inset is an image taken by selected-area electron diffraction (SAED) yielding a double six-spot-ring pattern; that confirms the benzene pattern of

graphene [17]. Figure 2.3B shows a wrinkled graphene film on top of the substrate observed by SEM.

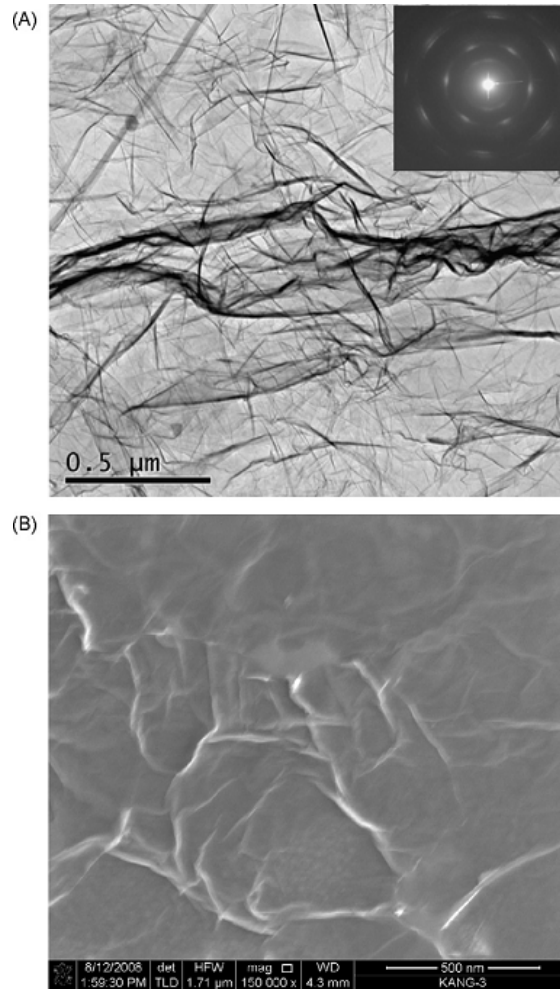


FIGURE 2.3: TEM (A) and SEM (B) image of a graphene flake [17].

The height of different graphene flakes was measured using the AFM (Fig. 2.4 shows an example of a graphene layer with 2 contacts observed using AFM), the graphene grown using CVD had height of 1.5 nm [10], the mechanically cleaved graphene's height was 0.8 nm [14–16], and from 3.5 nm to 5 nm corresponding to 7–10 layers of graphene [13].

2.2 Nanosensor types

Several types of sensors based on different detection mechanism are being used. Some are based on the change of resistance or operation frequency.

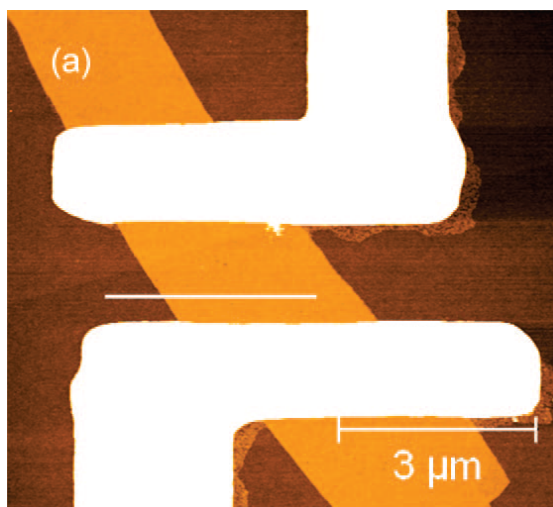


FIGURE 2.4: AFM image of a graphene device [14].

2.2.1 Resistive graphene-based nanosensor

Recently, the most common type of sensor is based on resistive response. The change of conductivity is measured after the exposure to the target molecules of gas or chemical vapor. The resistance-based sensor is easy to fabricate. The resistance is measured directly or from current/voltage characteristics between two contacts on top of a graphene layer [1, 12, 20–23]. Substrate plays an important role influencing graphene-based nanosensor properties [19]. For example, SiC dopes electrons into the graphene layer and makes it an n-type with a very low carrier concentration. In case of multilayer graphene sensor, however, the interlayer between the SiC and the surface, screens the effect of substrate and makes the sensor p-type with higher concentration of charge carriers.

2.2.2 Field effect transistor (FET) nanosensor

Source-drain current of the FET depends on the externally applied gate voltage. Adsorption of gas or chemical vapor molecules changes the carrier concentration, which can be measured in transistor-like devices [4, 19].

The detection levels of parts-per-million (ppm), or even a single molecule with fast response time, determine the graphene FET sensors to be a great choice for low cost commercial applications. Using pristine graphene showed a lower sensitivity compared to modified graphene as well as graphene with defects. Most effective for large-scale production with sufficient sensitivity proved to be using graphene

oxide and subsequently reducing it to obtain graphene for a graphene-based FET sensor [24].

2.2.3 Surface acoustic wave (SAW) nanosensor

The basic operation principle of a SAW sensor is that the resonance frequency (operation frequency) changes with adsorption of target molecules of gas or chemical vapor. In principle, it is a mass detection sensor, sensitive to change of mass caused by the adsorption of a target molecule. The shift in frequency is directly proportional to the mass of the gas or chemical vapor adsorbed on the surface. The basic device of a SAW sensor consists of a delay line with the propagation path covered with graphene which adsorbs the target molecules, causing a delay in the path and changing the frequency. SAW sensors can detect the change of mass and the change of surface conductivity. Acoustic wave velocity changes with a decrease in frequency caused by the adsorption of the gas or chemical vapor molecule [5, 25].

A graphene oxide-based SAW sensor's response to CO and H₂ was observed, and it can be concluded that exposure to CO decreased the frequency, on the opposite hand, the exposure to H₂ increased it. Since the mass of the H₂ molecule is 14 times smaller than CO, the main factor for H₂'s detection on graphene is the conductivity change, while in the case of CO it is the mass change.

2.2.4 Quartz crystal microbalance (QCM) nanosensor

Another type of a mass sensitive sensor is the bulk acoustic wave (BAW) sensor, in which the mass is detected by the corresponding shift of frequency, quite similar to the SAW sensor. Acoustic sensors are becoming more and more popular due to their high sensitivity and stability. Most popular BAW sensors are QCM sensors because even a small change in order of a nanogram in the electrode-mass can be detected. The additional mass changes momentum of the propagation of the acoustic wave and decreases the resonance frequency [6]:

$$\Delta f = -2.26 \times 10^{-6} f_0 \frac{\Delta m}{A} \quad (2.1)$$

where Δf is the resonance frequency shift, f_0 is the base resonance frequency for the QCM, Δm is the change of electrode-mass and A is the surface area of the electrode.

A graphene oxide-based QCM sensor was able to detect humidity changes in the range from 6.4 to 93.5 % at room temperature [6].

2.2.5 Micro electromechanical systems (MEMS) nanosensor

The MEMS is based on the CMOS technology, which has been recently used for sensor fabrication to miniaturize sensors and lower their energy requirements. The main features are fast response time, fast production and high sensitivity. First MEMS-based sensor was designed using a micro-hotplate based on CMOS processes [7]. The sensor consists of finger-like structure on micromachined silicon substrate with a controlled temperature using a micro-hotplate with graphene oxide films [26]. Current-to-voltage characteristics were found to be linear and ohmic in all cases. The resistance was found to be from 70 to 700 Ω depending on the number of layers and the distance between the electrodes. Sensors using monolayer of graphene show higher sensitivity and higher resistance.

The MEMS technology was also used in FET-based graphene sensors. Chen et. al., [27] shows that fabrication of back-gated graphene FET array on microchannels is possible (see fig. 2.5).

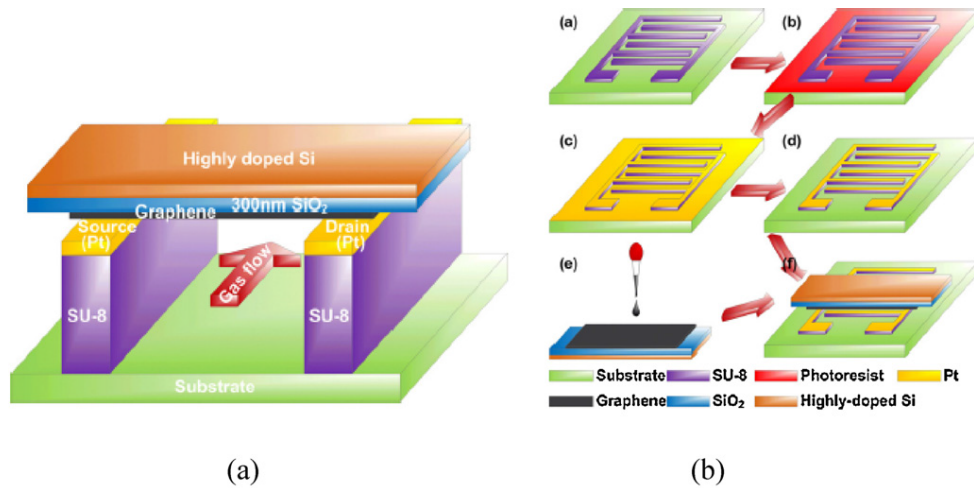


FIGURE 2.5: (a.) Scheme of the graphene FET. (b.) Fabrication process of the 3D graphene FET array [27].

2.2.6 Metal oxide hybrid nanosensor

Recently Yi et. al., [8] attempted to combine the advantages of conventional semiconducting metal oxides with graphene to improve its gas sensing properties. The sensor consisted of a metallic bottom electrode with vertically aligned ZnO nanorods deposited on top with graphene used as a top conductive electrode. They also demonstrated that the sensor can be bend below the radius of 0.8 cm and still show no mechanical or electrical failures. This kind of hybrid sensor shows promising results in selective detection of electron donor gases like CO and NH₃ and efficient detection of NO.

2.3 Graphene-based sensor fabrication methods

Prefabricated structures on top of the substrate are mostly used for easier orientation, localization of the graphene flakes on the surface of a sample and for the electrical connection of nanostructures, created using shadow mask with Cr/Au (10 nm / 250 nm) [19] or Ti/Au (3 nm / 60 nm) [11], and with prefabricated gold alignment markers [14, 16]. After the deposition of the graphene flakes, the electron beam lithography (EBL) [1] was used to pattern the conductive contacts between the localization structures and the graphene flakes. PMMA (polymethyl methacrylate) C4 950 [14, 15], or alternatively a double layer of PMMA A8 495 and PMMA A4 950 [16], tend to be used as the resist layer for the fabrication. The conductive metallic layer was sputtered using Ti/Au (5 nm/40 nm) [1, 12], Cr/Au (5 nm/50 nm) [14, 16] and suggested that by utilizing noble metals, the sensitivity of a graphene sensor can be enhanced, particularly with the use of Pd/Au (20 nm/80 nm) [13]. For an easy lift-off acetone is used, in some cases chloroform was used to dissolve all of the residual PMMA to prepare a clean surface. Chen [27] fabricated a 3D FET graphene sensor by deposition of a graphene layer on SiO₂/Si substrate by chemical reduction of graphene oxide. On separate substrate horizontal walls from SU-8 with metal layer on top were fabricated using standard lift-off process. Then they were pressed against the graphene layer in such a manner the electrodes create source and drain electrodes for the measurement. The SU-8 walls formed micro channels, which served as a passage for the gas and chemical vapors. This fabrication method avoided contamination of the graphene by resist residue.

After the EBL procedure graphene flakes showed evidence of contamination by a residual resist layer. The cleaning by heating the sample in flowing H_2/Ar at 400°C for 1 hour was proven to be effective in removing residuals of the resist [14].

The metal oxide hybrid sensor created by Yi [8] uses vertical ZnO nanorods on top of a metallic electrode using graphene as a top conductive electrode (Fig. 2.6).

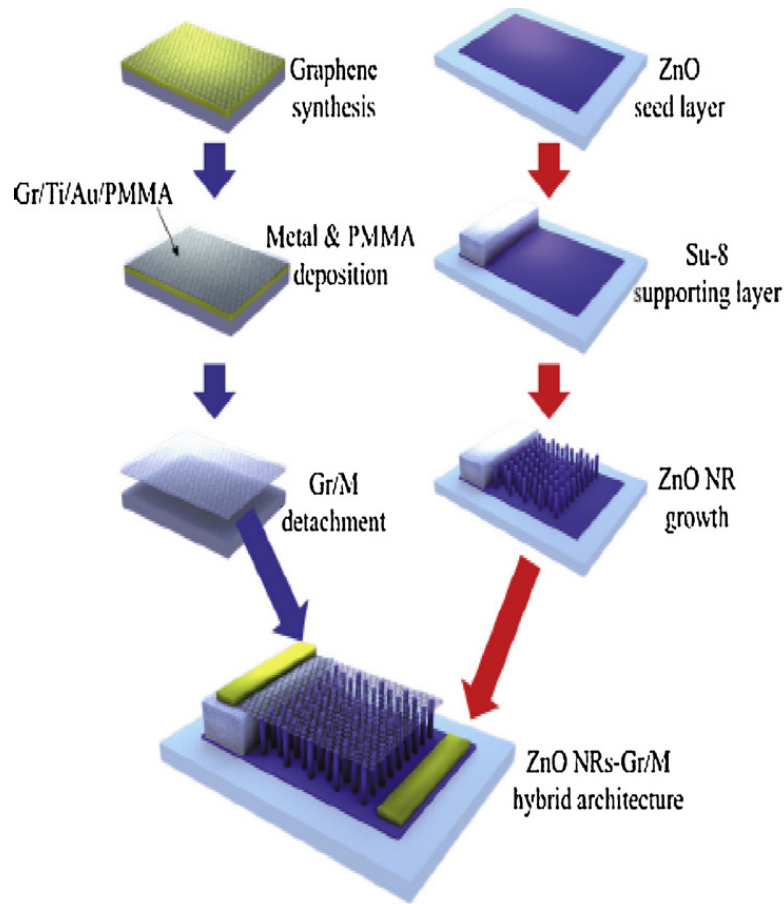


FIGURE 2.6: Scheme of the ZnO nanorod and graphene hybrid sensor fabrication [8].

2.4 Detection of Gas molecules

Individual gas molecules are detectable by sensors using graphene because of its main characteristics. Graphene is a two-dimensional material and has its whole volume exposed to surface adsorbents, maximizing their effect. As a highly conductive material graphene has rather low Johnson noise. A low level of excess ($1/f$) noise caused by thermal switching is very low due to graphene's few crystal defects. And the possibility to measure a four-probe method on a single-crystal with low

resistance contacts. All these characteristics maximize the signal-to-noise ratio, enabling the detection of concentration changes lower than one electron charge at room temperature [1].

One mono-layer and also several layers of graphene are able to detect gas molecules and have the appropriate resistance change [1]. Multilayers allow a much lower contact resistance ($\approx 50 \Omega$) in comparison with a monolayer ($\approx 4 \text{ k}\Omega$). The typical noise in such devices is $\Delta\rho/\rho \approx 10^{-4}$, which means a detection limit of 1 ppb.

The graphene used by Schedin et. al., [1] was in pristine state, using field-effect measurements at varying temperatures from 4 to 400 K in magnetic fields up to 12 T. This allowed to recognize a single, bi and multi-layer graphene and finding out the mobility of charge carriers mobility (μ) (typically $\approx 5000 \text{ cm}^2 \text{ V}^{-1} \text{ s}^{-1}$). Longitudinal resistivity exhibited a peak at zero gate voltage (V_g), indicating that the graphene is in its pristine, undoped state.

2.4.1 NO₂ detection

The devices were exposed to different concentrations of NO₂: strongly diluted in pure helium or nitrogen at atmospheric pressure (1 ppm) [1], a mixture of NO₂ and carrier gas of N₂ and 20 % O₂ [19], diluted in N₂ (100 ppm) [12] and varying from 100 ppm up to 500 ppm in the air [13] at room temperature. The graphene reacts to even small concentrations of NO₂ very quickly as seen in the Figure 2.7, however, the desorption of NO₂ from the surface is very slow. Figure 2.8 shows the same response at zero electric-field. In region II we can see rapid change in the resistivity, after some time it is followed by a region of saturation with very slow change of resistivity. The evacuation of the gases led only to a small change of resistivity, suggesting very strongly attached adsorbed gas molecules on the surface of graphene. The initial state was recovered by annealing at temperatures of 140 – 150 °C in vacuum (Fig. 2.7 part IV). UV illumination for a short periods of time had the same effect as thermal annealing [1, 13].

The most important requirement on a gas detector is reproducibility. The graphene-based nanosensors were repeatedly exposed to NO₂ and air to study any deterioration caused by any gas molecules not desorbed from the surface. All the

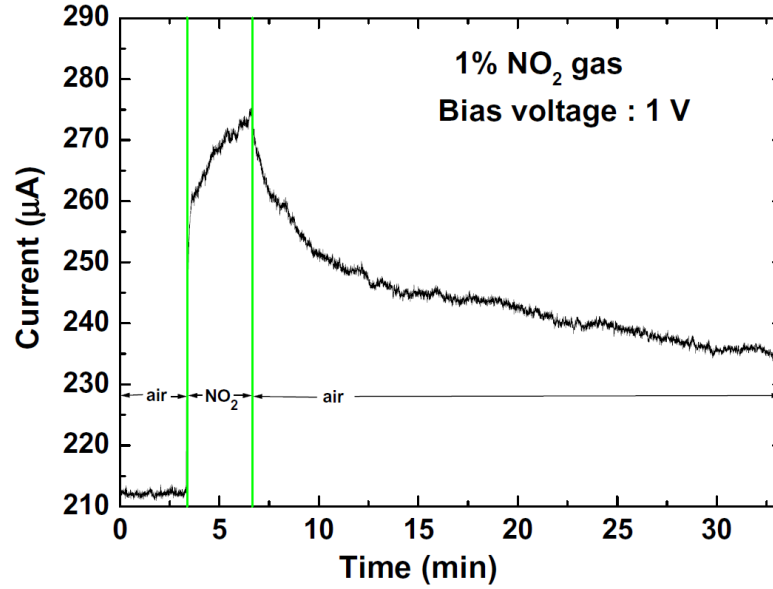


FIGURE 2.7: The time response and decay of graphene-based gas using and ambient NO_2 concentration (1 %) [13].

experiments from references [1, 12, 13] suggest no change in sensitivity of the device as can be seen in Figure 2.9. The sensitivity can be defined as:

$$S(\%) = \frac{R_{Air} - R_{NO_2}}{R_{Air}} \times 100\% \quad (2.2)$$

where R_{Air} and R_{NO_2} are graphene resistance in air and NO_2 gas. Sensitivity reported for 100 ppm was 9 % and for 500 it was 14 % [13].

The NO_2 gas acts as an acceptor on the surface of the graphene.

2.4.2 H_2O detection

Graphene can be prepared as with hydrophilic (GO) but also with hydrophobic (rGO) properties [28]. Bi et. al. [29] show that the sensitivity of a graphene oxide sensor to humidity is higher than the sensitivity of exfoliated and CVD graphene, making the graphene oxide a viable material for humidity sensors [30]. Water vapors on the graphene surface act as acceptors, increasing the sensor conductivity. Figure 2.8 shows a response of the graphene to water vapors, but also as in the case of NO_2 , water vapors are strong adsorbate on the surface of graphene. For a reproducible measurement the device has to be annealed in vacuum or UV illuminated to desorb the molecules. Dan et. al. [14] observed dramatic changes in the electrical response after the cleaning procedure, heating in H_2/Ar at 400°C

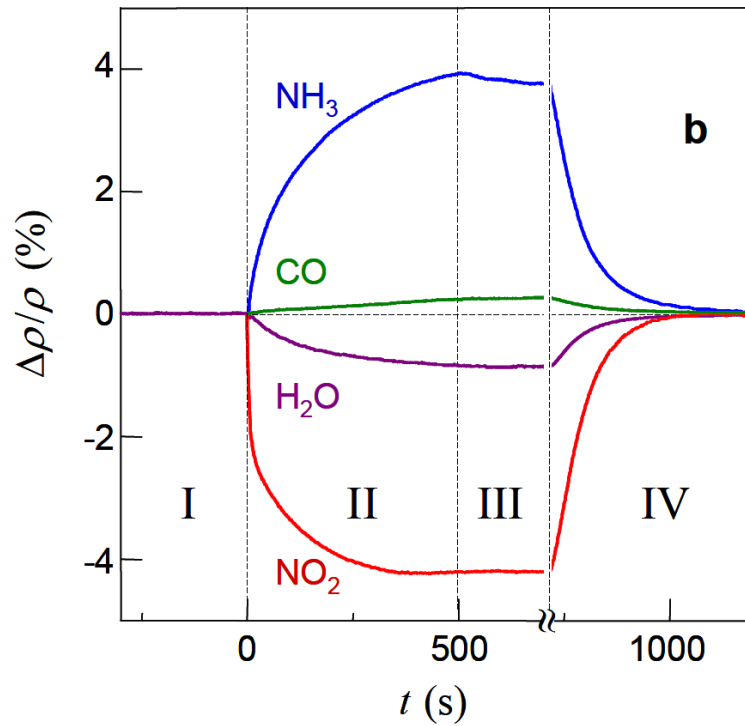


FIGURE 2.8: Graphene is exposed to gases diluted in concentration of 1 ppm. Region I – in vacuum, II – exposure to gases, III – evacuation of the gases and IV – annealing at 150 °C [1].

for 1 hour to get rid of the resist residues. Figure 2.10 illustrates the difference in the response of the graphene sensor before (black line) and after cleaning (red line). The responses decrease sharply in the clean samples, suggesting a functionalization of the sensor using the residual resist contamination [14].

2.4.3 CO₂ detection

Yoon [16] exposed the graphene sensor to CO₂ at different temperatures. Figure 2.11a shows the conductance response of the graphene nanosensor on the presence of CO₂ in time at 22, 40 and 60 °C. After 30 seconds, 100 ppm of CO₂ was let into the chamber, quickly increasing the conductance of the graphene. After a short time the conductance reaches a stable value. The change of conductance indicates a charge transfer between the CO₂ molecule and the graphene, showing that the physical adsorption of the CO₂ molecule is the dominant sensing mechanism. After the supply of the gas was cut off, the sensor is recovered in a few seconds (around 10 s), meaning the interaction between CO₂ and graphene is very different compared to NH₃ or NO₂. The sensor does not require high temperature

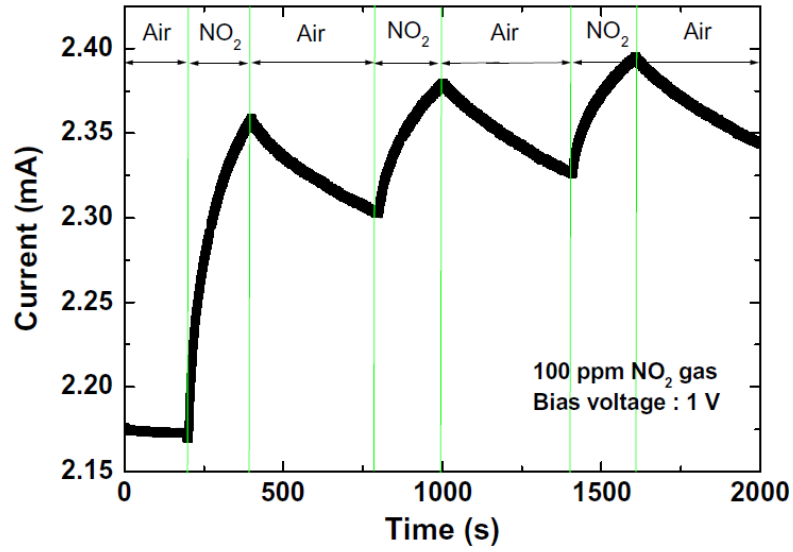


FIGURE 2.9: The reversibility for the graphene device using NO₂ (100 ppm) and air [13].

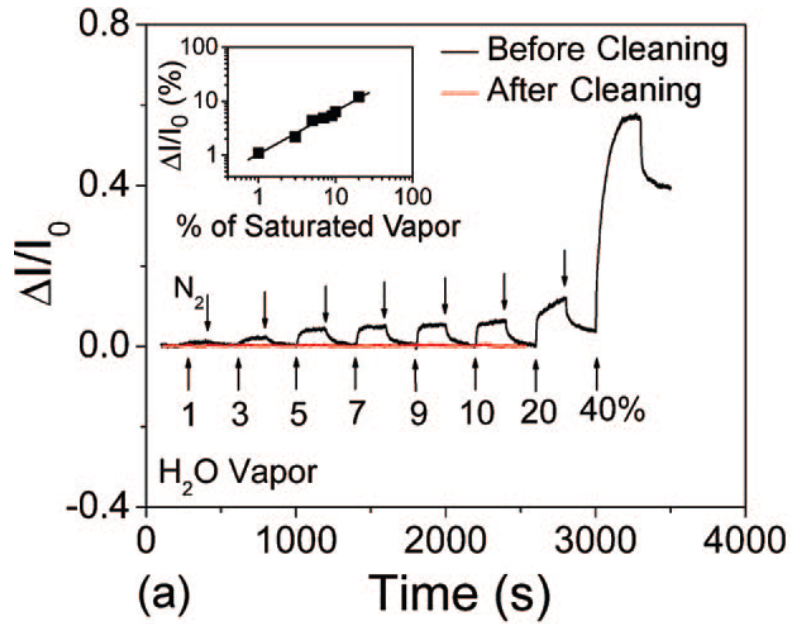


FIGURE 2.10: Measured sensor response before (black) and after (red) sample cleaning [14].

annealing in vacuum to desorb all of the molecules. Figure 2.11b shows the ratio between the conductance change and the CO₂ concentration. The estimated sensor sensitivity for CO₂ was 0.17%/ppm for concentrations from 10 to 100 ppm of CO₂ gas.

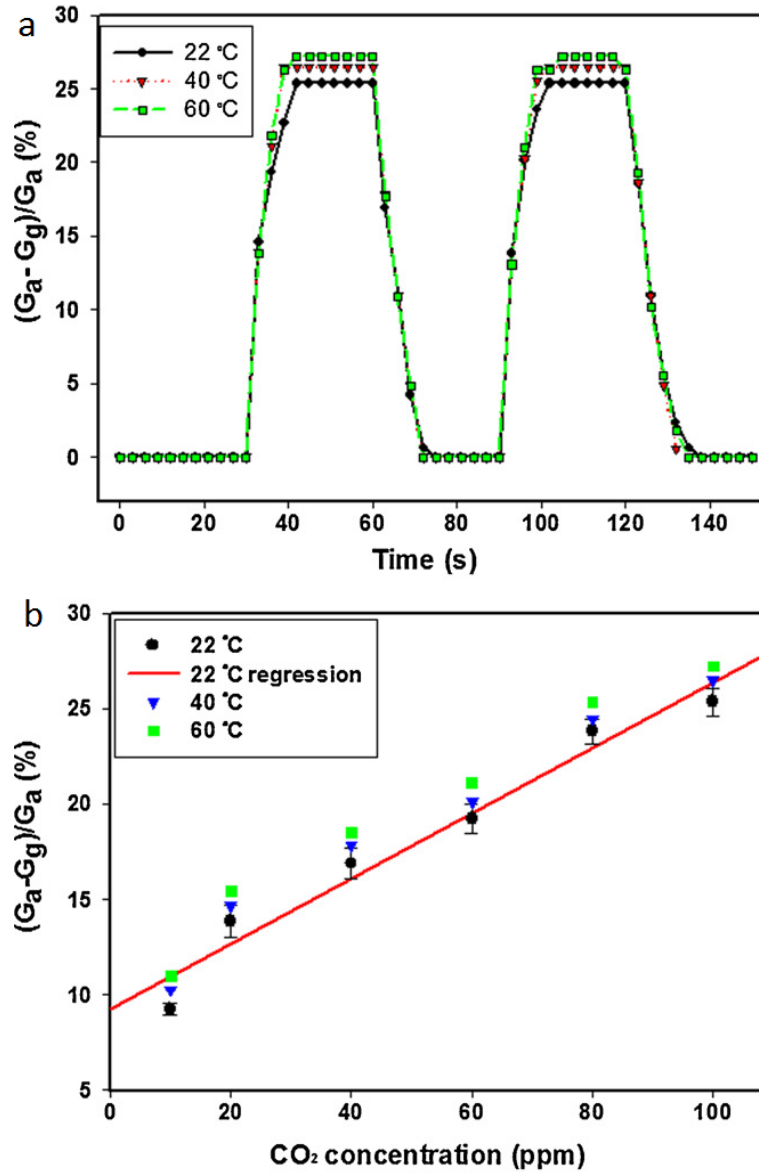


FIGURE 2.11: (a) Time response of the graphene CO₂ gas sensor in the presence of 100 ppm CO₂, at different temperatures; (b) changes of conductivity as the function of CO₂ concentration [16].

2.4.4 Impurities

The V-shaped $\sigma(V_g)$ —curves characteristic for graphene (Fig. 2.12), more importantly their slopes, suggest that the chemical doping did not affect scattering rates. Analysis of the chemically-induced ionized impurities performed by Schedin F., et. al., [1] in graphene for concentrations $>10^{12} \text{ cm}^{-2}$, indicates that charged impurities should not limit the mobility (μ) until it reaches $\approx 10^5 \text{ cm}^2 \text{ V}^{-1} \text{ s}^{-1}$. This is in contrast with another 2D system in which such high densities are destructive

for the ballistic transport. All these observations suggest that charged impurities are not the current limiting factor for μ in graphene.

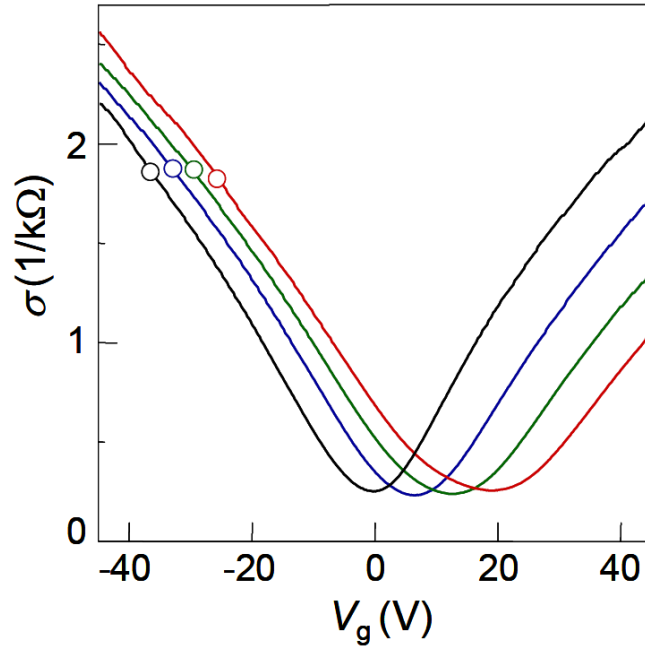


FIGURE 2.12: Conductivity σ of single-layer graphene away from the neutrality point changes approximately linearly with increasing V_g [1].

2.5 Doping of graphene

The type and concentration of charge carriers can be controlled by changing the gate voltage or dopant concentration [12]. In Figure 2.13 we can see the change of the resistivity in graphene depending on the applied gate voltage, shifting the Fermi level below/above the Dirac point with the negative/positive gate voltage. As was previously said, the graphene with its honeycomb lattice can be doped heavily without a significant loss of mobility. Adsorbed gas molecules on the graphene's surface act as donors or acceptors, thus changing the electrical conductivity σ of graphene. Even one gas molecule interacting with the surface changes the local carrier concentration, which leads to step-like changes in resistance. Based on the highest occupied molecular orbital (HOMO) and lowest unoccupied molecular orbital (LUMO) of the adsorbed gas molecule we can distinguish two charge transfer mechanisms. If the HOMO/LUMO of the adsorbate is above/below Dirac point, there is a negative charge transfer to/from graphene. Hybridization between HOMO and LUMO of the adsorbate with the graphene orbitals partially

influences the charge transfer between the gas molecule and graphene [31]. Most focused gas molecules are nonmagnetic H_2O , NH_3 and CO , followed by paramagnetic NO_2 and NO . As shown in Figure 2.14 there are 3 different position for the gas molecule to be adsorbed on the surface of graphene and each molecule can have different orientations in each position. Table 2.1 shows different gas molecules and their effect on the graphene with their orientations. In conclusion with the reference [31] the adsorption site changes the doping only slightly on the other hand the orientation of the gas molecule influences the doping strongly.

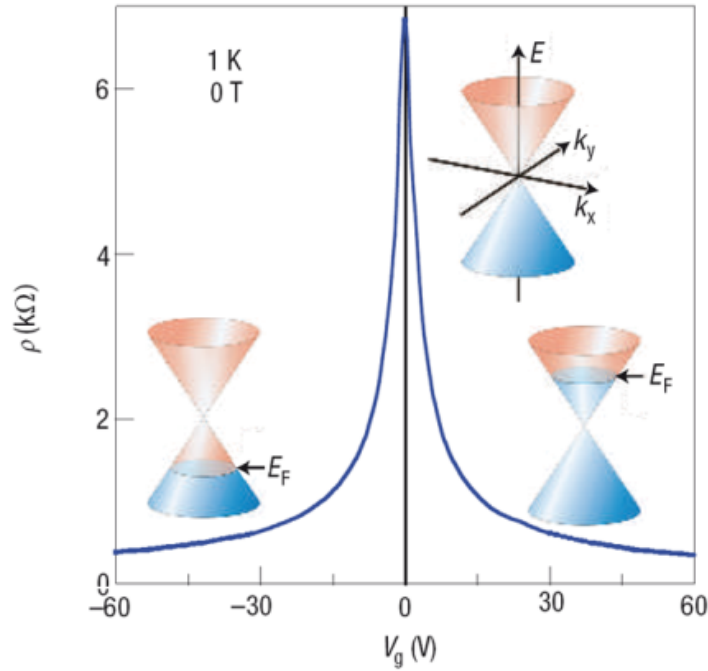


FIGURE 2.13: Ambipolar electric field effect in single-layer graphene. The insets show its conical low-energy spectrum $E(k)$, indicating changes in the position of the Fermi energy E_F with changing gate voltage V_g . Positive (negative) V_g induce electrons (holes) in concentrations $n = \alpha V_g$ where the coefficient $\alpha \approx 7.2 \times 10^{10} \text{ cm}^{-2}/\text{V}$ for field-effect devices with a 300 nm SiO_2 layer used as a dielectric. The rapid decrease in resistivity ρ with additional charge carriers indicates their high mobility (in this case, $\mu \approx 5000 \text{ cm}^2/\text{Vs}$ and does not noticeably change with temperature up to 300K) [32].

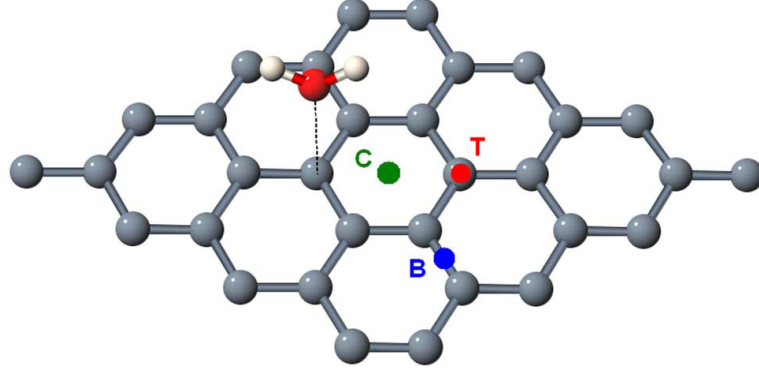


FIGURE 2.14: 4×4 super-cell of graphene with the adsorption positions C (Center of the honeycomb), T (Top of the C atom) and B (Between the C atoms), with H_2O molecule [31].

Adsorbate	Doping	ΔQ [e]	Orientation
H_2O	Acceptor	-0.025	First O–H bond paralel to the surface Second O–H bond pointing to the surface
NH_3	Donor	0.027	H atoms pointing away from the surface
CO	Donor	0.012	C–O bond almost paralel to the surface
NO_2	Acceptor	-0.099	N–O bonds pointing to the surface
NO	Donor	0.018	N–O bond almost paralel to the surface

TABLE 2.1: Gas molecules on graphene surface doping as acceptors or donors, with the charge transfer from the molecule to graphene (ΔQ) and their orientation.

Chapter 3

Experimental setup

3.1 Design of structures for transport measurement

It is very important to have a suitable configuration of electrodes for transport properties measurement of graphene/graphite layers. They can be measured in a 2-point probe or a 4-point probe configuration, depending on the performed type of measurement. Using a 2-point probe configuration, the resistance of graphene can be measured easily and directly, however, the added resistance of the contacts is included. The 4-point probe configuration allows to measure the resistivity of the layer without the resistance of the contacts, but it needs a defined configuration of contacts and the knowledge of the surface area.

3.1.1 2-point probe structures

Previously, the most significant problem related to graphene nanostructures transport measurement consisted in the fact that all of them were destroyed after the connection of the wires and applying the voltage. This problem was contributed to the residual PMMA (poly methyl methacrylate) left on top of the graphene layer after the electron beam lithography used for fabrication of top contacts. Following the deposition of gold contacts, PMMA was found between the graphene and the gold contact, increasing the resistance of the contact and heating up the graphene layer.

To overcome this problem, the gold contacts were fabricated before the exfoliation of graphene on them. Since PMMA does not leave any residue on top of gold contacts, and can be easily removed from the SiO_2 surface using acetone and plasma etching, there is no graphene/PMMA/gold interface to interfere with the resistance measurement.

Figure 3.1 shows interdigitated finger electrodes with bond pads designed for the 2-point probe measurement, taking into consideration the random dispersion of graphene flakes on the sample surface during exfoliation.

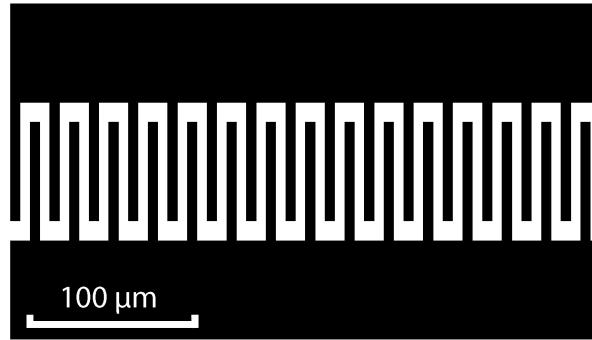


FIGURE 3.1: Interdigitated finger-like electrodes for 2-point probe measurements with bond pads.

3.1.2 4-point probe structures

For 4-point probe measurements it is not possible to design an array of electrodes relying on the random dispersion of graphene flakes during exfoliation. Such structures would be too complicated to fabricate and would have a low success rate of graphene layer sticking to all four required contacts.

Structures with universal array of electrodes were designed to fulfill all the needs to create four or more contacts for a 4-point probe transport measurement (see fig. 3.2). Five big bonding pads were developed with dimensions $100\text{ }\mu\text{m} \times 150\text{ }\mu\text{m}$ on each side of the square, with alignment symbols in each corner and small marks inside the structure, to be used during subsequential electron beam lithography to create the contacts between a graphene flake and bonding pads.

In this kind of structures the graphene/PMMA/gold interface is not excluded, hence the lithography process needs to be altered using special PMMA (lower molecular weight) to overcome the problem.

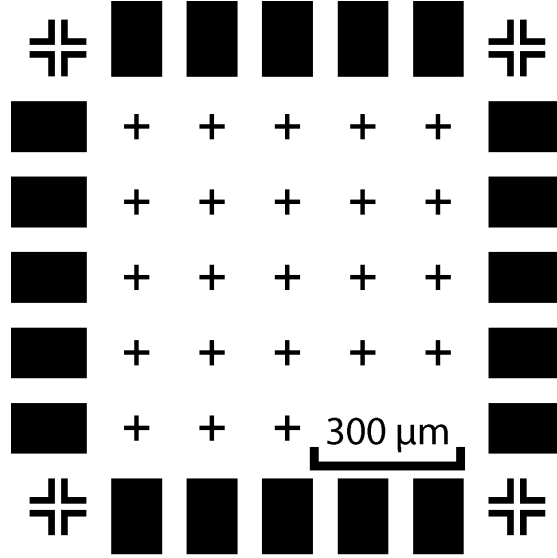


FIGURE 3.2: Universal array of electrodes for 4–point and 2–point probe transport measurements.

3.1.3 Sample holder

In cooperation with the Department of Microelectronics (Faculty of Electrical Engineering and Communication, BUT) sample holders for the transport measurements were designed and fabricated. Ceramic plate with conductive contacts and bonding pads on one end, and pins for cables on the other. A big conductive electrode was situated in the middle, for the sample to be placed in and glued to it with conductive silver paste, and used for a back gate electrode (see Fig. 3.3).

3.2 Fabrication of structures for transport measurement

The whole process starts with cutting silicon wafer with thermally grown layer of silicon dioxide, the thickness of SiO_2 is ≈ 280 nm, into samples of a rectangular shape with dimensions $\approx 1 \text{ cm} \times 1,5 \text{ cm}$. Their size is slightly bigger than what is necessary for the structures designed for 2–point and 4–point probe measurements, but the additional edge was necessary because the samples would undergo a lot of different fabrication and measurement processes, so there was a substantial chance of cleaved edges which could damage the structures.

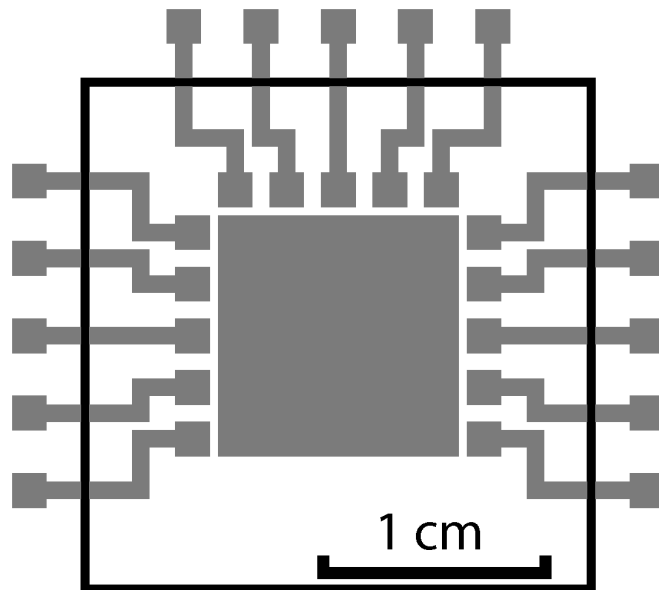


FIGURE 3.3: Sample holder with one big central electrode and conductive contacts with bonding pad on one end and pin for cables on the other.

3.2.1 Spincoating of PMMA

Electron beam lithography (EBL) requires a suitable resist; this case a positive resist 495 PMMA A4 (495 000 is the molecular weight of the polymethyl metacrylate and A4 denotes concentration of 4% solution in anisole). The term positive resist means that any area which was exposed to electron beam would be washed away, because an exposure to electron beam causes the molecules to untangle.

The whole process starts with acetone, isopropyl alcohol and demineralized water bath, followed by plasma etching to ensure that the surface of the sample is clean of any unwanted organic or inorganic matter. In the following step, a process called spincoating is utilized to deposit a thin layer of material onto a sample surface using high speed spinning[33]. Figure 3.4 shows the dependency of the PMMA height on the spinning speed during the process.

The sample has been blown with nitrogen to ensure there are no dust particles on the surface before the resist is applied. After the prebake at 180 °C, usually 35 μ l of 495 PMMA A4 is used for each spincoating. The spincoating process consists of 2 steps: 30 seconds at 500 rpm and 50 seconds at 4000 rpm, making the height of the resist \approx 180 nm, after which the sample is postbaked for 90 seconds to harden the resist.

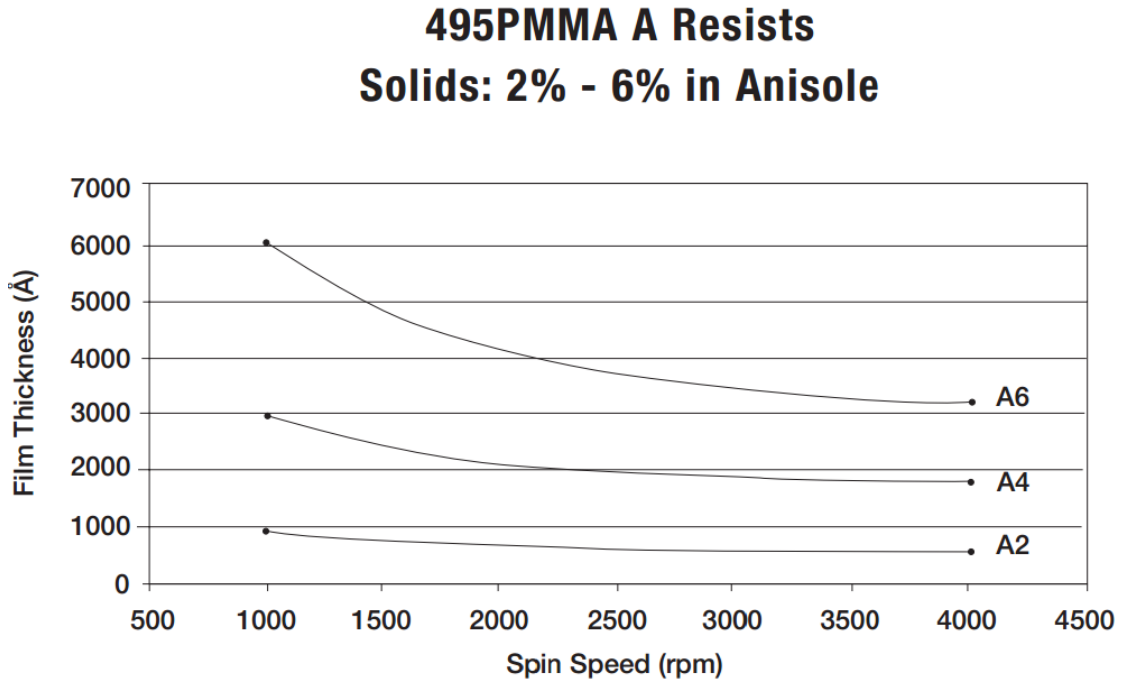


FIGURE 3.4: Dependence of the PMMA height on the spin speed for 3 different concentrations A6, A4 and A2 [33].

The same procedure is used to create the contacts for the 4–point probe, but with another resists. Because the resist comes into contact with the graphene flakes, a special PMMA was picked up with the molecular weight of only 50 000 (50 PMMA A3), which should leave no residue after the electron beam lithography on top of the graphene layer. The whole layer of resists is a sandwich of 50 PMMA A3 and 495 PMMA A4, because only one layer of 50 PMMA A3 would not be enough for electron beam lithography.

3.2.2 Electron beam lithography

Since UV lithography could not be used for fabrication of big nanostructures presented in this work, the electron beam lithography was utilized to create both the big and small structures. For bigger structures the UV lithography is the better option because it is much faster with resolution down to 2 μm ; to expose any structure with critical dose it takes in order of seconds compared to electron beam lithography's 40 minutes up to 7 hours.

Usually the electron beam lithography is carried out by an electron lithograph or a modified scanning electron microscope with the possibility to control the movement

of the beam on the sample surface with a pattern generator. The scanning electron microscope consists of an electron source, electron optics and a sample chamber.

Most used electron sources are thermal emission, cold field emission and Schottky cathode. Thermoemission cathode has high current stability but it is very difficult to focus the beam into a small spot and get a good resolution because the high chromatic aberration. The main advantages of autoemission cathode is high emission current density, small beam spot and low chromatic aberration, but the overall emission current is very low making it unsuitable for lithography. On the other hand the Schottky cathode has high overall emission current with small beam spot making it ideal for lithography.

After the emission from the electron source, the electrons are accelerated and focused with the electron optics. Scanning electron microscopes have deflection electrodes to allow the beam to scan the surface; in comparison, with a scanning electron microscope suitable for lithography has to have a fast possibility to deflect the electron beam outside the sample, so called beam blanker. The electron optics providing the possibility of magnification is present to correct the aberrations of the electron source and the optics itself. Uncorrected electron beam affects the quality of the final structure. The main aberrations which have to be corrected are: spherical, astigmatism and chromatic.

Interaction of the electron beam with resist leads to untangling of the molecular bonds, in case of the positive resist, and allows to be washed away by the developer. Every resist has its critical dose (units $\mu\text{C cm}^{-2}$), it is the maximum of exposed energy which causes the breakdown of the molecular bonds of the resist with contrast defined as [34]:

$$c = \log \frac{D_1}{D_2} \quad (3.1)$$

in which D_1 is the highest dose, not to cause any modification of the resist and D_2 is the lowest dose which causes the complete removal of the resist. With acceleration voltage of 30 kV the dose D_2 is $\approx 350 \mu\text{C cm}^{-2}$.

More advanced lithography software already has an optional proximity effect correction, simulating the effect and changing the exposition dose in different areas of the structures. Proximity effect are backscattered, and secondary electrons from the substrate or resist causing the secondary exposition of the resist and corruption of the structure geometry.



FIGURE 3.5: Scanning electron microscope Lyra 3 XMH from Tescan. The opened sample chamber with motorized XYZ stage [35].

All of the lithography structures were created using Lyra 3 XMH FIB–SEM from Tescan (see Fig. 3.5), with Schottky cathode as the electron source with the possibility to achieve beam spot diameter of few nm. The microscope offers the possibility to change the acceleration voltage between 1–30 kV and uses a motorized XYZ stage. Lyra uses specialized lithography software from Tescan called Drawbeam, creating each planar structure from series of lines with the distance between each spot in the line as a multiple of the theoretically calculated beam diameter.

Before the electron beam lithography procedure, the electron beam was focused and calibrated on a calibration sample containing gold islands on top of a carbon substrate. After the beam was properly calibrated, the overall emission current was measured using a Faraday cell (one of the parameters of EBL is the current) for several beam intensities. After that, the sample was moved into the position and the beam was focused on the surface of the sample, usually some contamination in the resist or a scratch is left on the SiO₂ surface (there is always a small height difference between the calibration and lithography sample, that is why the beam has to be refocused). In the next step the structures were created in the Drawbeam

software, the critical dose was set (several layers with different critical doses can be created), and the lithography process was engaged.

The first structure for electron lithography fabrication can be seen in Figure 3.6 a, the distance between each finger-like electrode is $6\text{ }\mu\text{m}$, not to cause any problems during lift-off, but still enough to have a mid-probability of graphene flake landing on top of at least 2 of them during exfoliation. The distance between the bonding pads with the dimensions of $100\text{ }\mu\text{m} \times 500\text{ }\mu\text{m}$ is $300\text{ }\mu\text{m}$. The 495 PMMA A4 resist spincoated at 4000 rpm was used to get the height of $\approx 170\text{ nm}$ and critical dose of $240\text{ }\mu\text{C cm}^{-2}$ (the critical dose was optimized using several layers with the same structure but different doses to optimize the contrast of the structures).

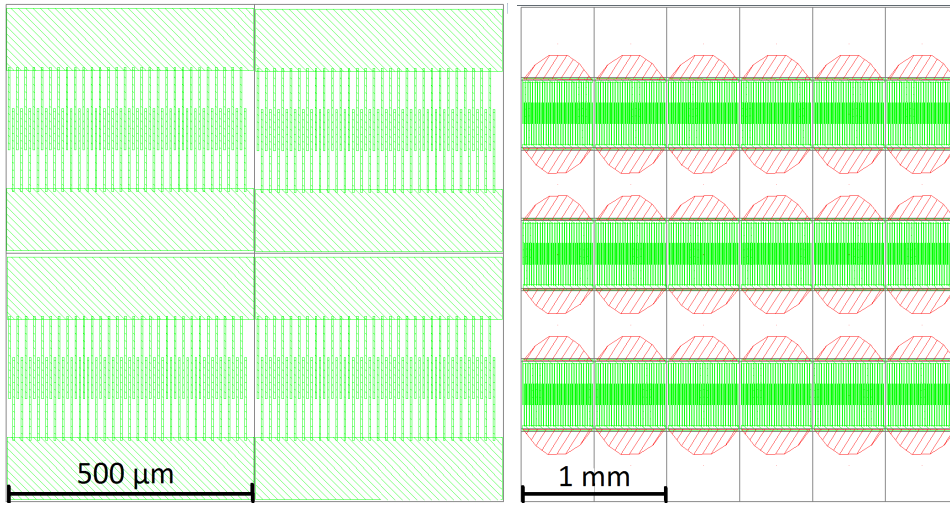


FIGURE 3.6: a) first structure created using electron beam lithography with $6\text{ }\mu\text{m}$ distance between each finger like electrode and the distance between bonding pads of $300\text{ }\mu\text{m}$, b) second structure with the same distance between the finger electrodes as in first structure but with different distance of $500\text{ }\mu\text{m}$ between the bonding pads and shape.

The second structure (see fig. 3.6 b) was created to cover larger areas of the sample to maximize the chance of a graphene flake landing between the two opposite finger-like electrodes but still keeping each structure independent on each other. The distance between the finger-like structures is the same as in the case of the first structure, but it contributed to changes in distance between bonding pads up to $500\text{ }\mu\text{m}$ and their shape. The finger-like electrodes are in the green layer with dose of $240\text{ }\mu\text{C cm}^{-2}$ and the bonding pads are in the red layer with dose of $200\text{ }\mu\text{C cm}^{-2}$ using 495 PMMA A4.

Lastly, the third structure (see fig. 3.7) was created with two big bondings pads in a separated red layer, connecting several fields of structures based on the first

structure in the green layer. The distance between the finger-like electrodes in the green is the same $6\text{ }\mu\text{m}$, with the distance between the interconnecting electrodes of $300\text{ }\mu\text{m}$ with dimension of $20\text{ }\mu\text{m} \times 500\text{ }\mu\text{m}$. The red layer contains the bondings pads and electrodes connecting the fields of finger-like structures. The dose for the green layer was $240\text{ }\mu\text{C cm}^{-2}$ and for the red layer the dose of $200\text{ }\mu\text{C cm}^{-2}$ – almost the same as in the first two cases with proximity effect correction.

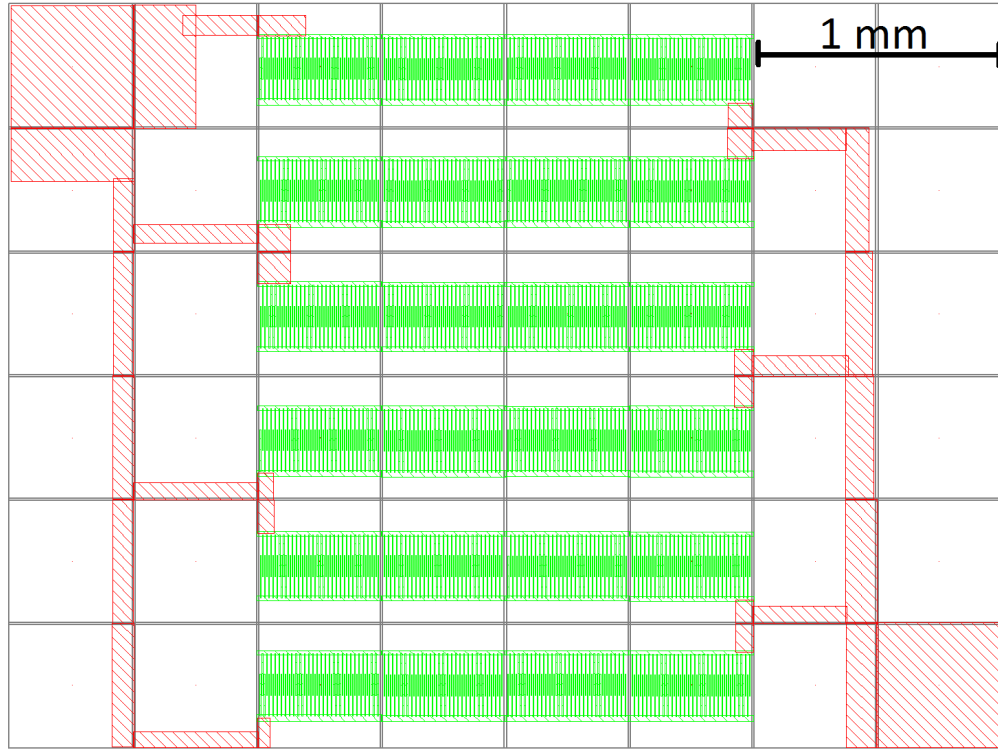


FIGURE 3.7: Third kind of structure with 2 big bonding pads and field of finger-like electrodes with the distance of $6\text{ }\mu\text{m}$.

The 4-point probe measurement requires different structures, therefore, the universal structure was created as shown in Figure 3.8: the array of nine systems with 20 electrodes and alignment marks. The green layer consists of electrodes with dimensions of $100\text{ }\mu\text{m} \times 150\text{ }\mu\text{m}$, alignments marks and position system require the dose $200\text{ }\mu\text{C cm}^{-2}$ for the array. The small position marks and the numbers inside the system of electrodes belong to the red layer with dose of $240\text{ }\mu\text{C cm}^{-2}$ using 495 PMMA A4.

The position marks and the numbers inside the system of electrodes is for identifying the graphene flakes after exfoliation and during the second lithography process. The electrodes dimensions were chosen to be capable of being used as bonding pads in the later stages of sample fabrication.

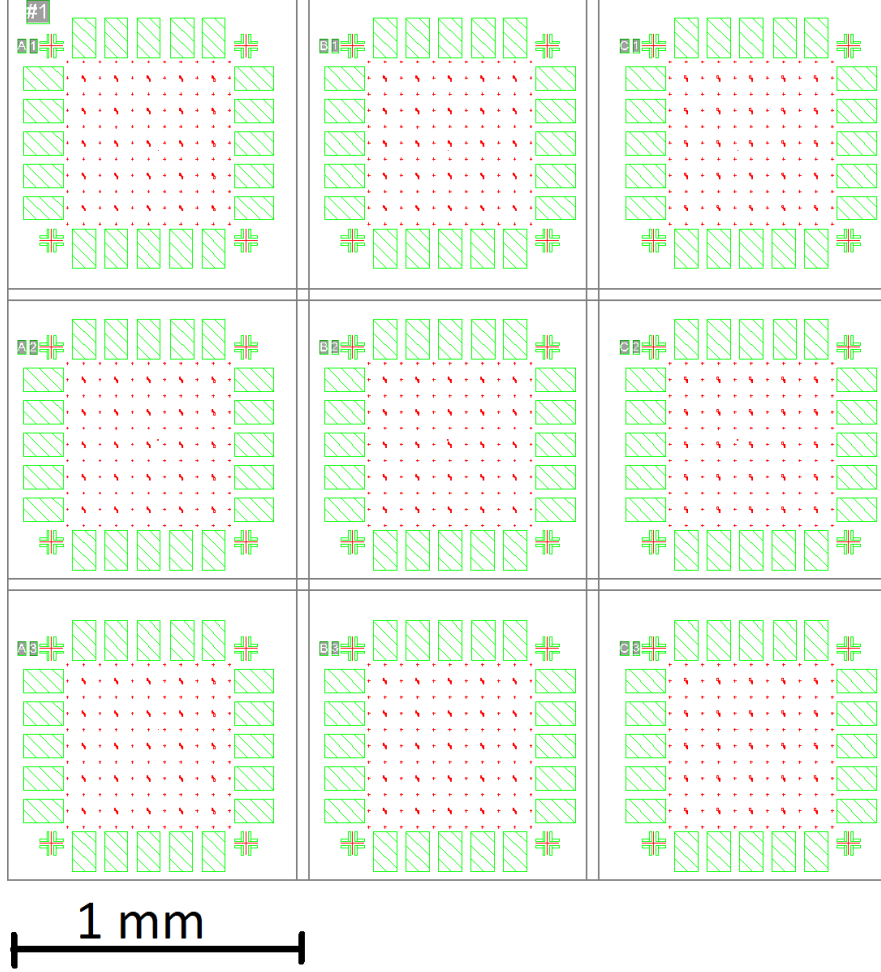


FIGURE 3.8: Universal structure with nine systems, each of them contains 20 big bonding pads and alignment marks.

The universal structures require a second lithography process – after the exfoliation and identification of graphene flakes on the sample surface – to connect the graphene layers with bonding pads. First pictures of the graphene flakes were taken (as an example see fig. 3.9) to be used for the alignment with the already existing structures on the substrate surface (only gold electrodes are visible under the layers of resist). After that the sample was heated up to 180 °C for an hour to evaporate all of the remaining water on the substrate surface, since the remaining water vapor lowers the adhesion between the sample surface and the resist and can cause non-adhesion. Followed by the spincoating of 2 layers of 50 PMMA A3 and 1 layer of 495 PMMA A4, the sample was baked for 90 seconds at 180 °C.

As in the case of the previous structures, the beam has to be focused and corrected before starting the actual lithography. However, during the measurement of the overall beam current in the Faraday cell, not only the current for the beam used

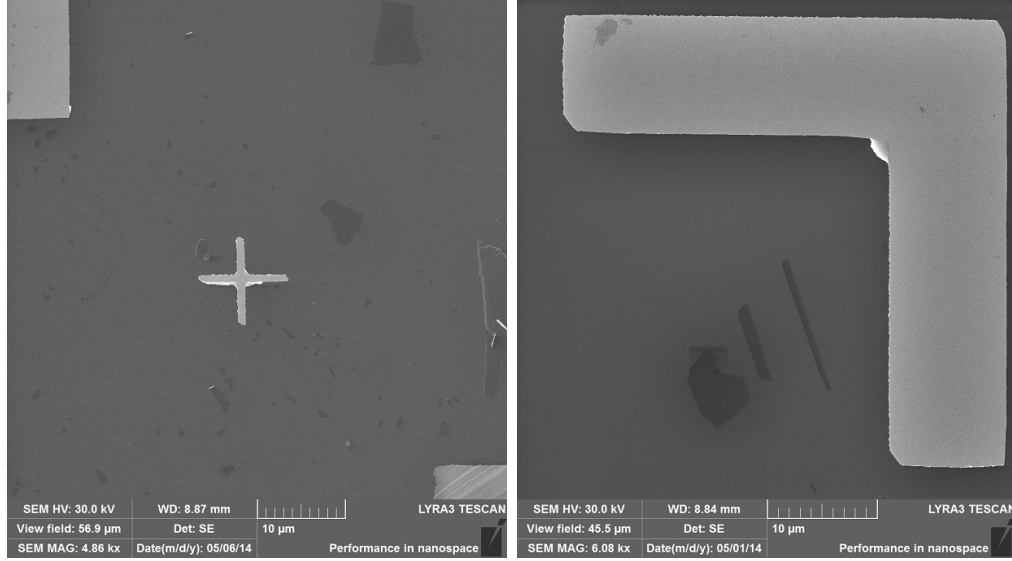


FIGURE 3.9: Two examples of graphene layers with alignment marks imaged by scanning electron microscope.

during the lithography has to be found, but also a beam intensity for observing and aligning the sample with the mask has to be found. The current must be low enough not to expose the resist, but high enough to have a good theoretical beam spot diameter. After all these criteria are met, the sample is moved into the position and the beam is refocused on the surface of the sample. The correct position has to be found using the bonding pads and the alignment marks with the help of a selective scanning window, only parts of the scanned area are exposed (to avoid critical exposure of the resist) and used for alignment of the mask with the previous structures.

Figure 3.10 a) shows small contacts only $0.7\ \mu\text{m}$ wide (the smaller one on the left of the graphene flake), and bigger contacts used for source and drain wide $1.5\ \mu\text{m}$. The alignment mark in the right top corner was scanned using the selective scanning window so the same structure on the imaged (which can be still seen) can be synchronized with it. When everything is ready the contacts are drawn and exposed using the critical dose of $220\ \mu\text{C cm}^{-2}$ (the resist was already exposed during the process of aligning the sample and image, so the critical dose is lowered not to overexpose the structures), and the proximity effect corrected. Bigger contacts between the bonding pads and smaller contacts are $4\ \mu\text{m}$ wide and created using critical dose of $180\ \mu\text{C cm}^{-2}$ (bigger structures require smaller critical doses).

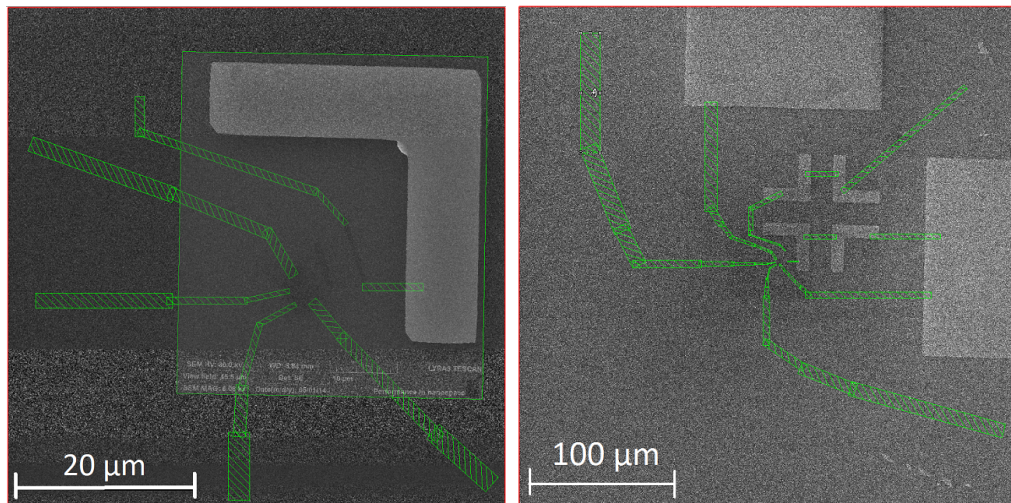


FIGURE 3.10: a) Fabrication of small contacts on top of a graphene flake, the width of the contacts on the left is $0.7\mu\text{m}$ and the bigger contacts used for source and drain are $1.5\mu\text{m}$ wide. b) Contacts connecting the bonding pads and smaller contacts created previously.

3.2.3 Development of the exposed structures

Usually a 1:3 solution of methyl isobutyl ketone (MIBK) and isopropyl alcohol (IPA) 1:3 is used for development of the exposed PMMA films. In case of this work a solution of IPA and demineralized water was used in ratio 7:3 due to its superior lateral resolution. Each layer was being developed for 90 seconds in this solution, washed in demineralized water and blown dry in nitrogen to ensure that all of the solution is removed, because the whole layer is dissolved: the exposed area dissolves much faster than the area which was not exposed, but the unexposed area is still dissolved over time in the developer. After the development, the etched areas of the resist can be observed using optical microscope in bright and dark field mode.

3.2.4 Ion beam deposition

The sample with the developed resist is moved into a vacuum chamber in which a metallic layer is deposited. The ion beam deposition technique was used to deposit a 3 nm thick layer of titanium (for better adhesion of the gold on top of SiO_2) and a 60 nm thick gold layer.

3.2.5 Lift–off process

After the metallic layer has been deposited, the remaining resist has to be removed from the sample surface. A process called lift–off is used for this purpose. First the whole sample is dipped in a solvent (mostly acetone) for several hours or even days. In the areas where the metallic layer touched the surface, the gold contacts will remain and only the areas in which the metallic layer was on top of the resist will be dissolved. The sample is washed with a constant stream of the acetone until last residues of resist are gone and then transferred into a neutralizer (mostly IPA) and washed in demineralized water and blown dry using nitrogen. The whole lift–off process can be accelerated using warm acetone (safely up to 40 °C) or using an ultrasonic cleaner, but it may cause the damage of the structures.

3.2.6 Summary of the metallic contacts fabrication

Since the fabrication procedure consists of many steps, a small summary of the processes used so far is repeated. Firstly, the whole process starts with cutting and cleaning a Si substrate with a layer of SiO₂ (see Fig. 3.11 a), followed by a spincoating of PMMA resist on top of the substrate surface (Fig. 3.11 b). After a successful spincoating the sample is put into a scanning electron microscope and exposed to electron beam through a predefined mask (see fig. 3.11 c), followed by ion beam deposition of metals (Fig. 3.11 d) and lift–off process in acetone (Fig. 3.11 e). The final result is a clean structure without rough edges (see Fig. 3.11 f).

3.3 Graphene exfoliation

Before the exfoliation, the surface was etched using plasma etching (80 % Ar to 20 % O₂ at 0.5 mbar), which not only cleaned the surface, but also modified the gold properties to hydrophilic (in case of finger–like structures there was a problem with sticking of the graphene flakes between the hydrophilic gold finger–like electrodes), improving the number of graphene layers exfoliated between at least 2 finger–like electrodes. The graphene was exfoliated using scotch tape method as shown in Figure 3.12; the process starts with a low adhesion scotch tape on which a small piece of highly–ordered pyrolytic graphite (HOPG) is placed. After the piece of HOPG is removed from the surface, the tape is overlaid several times to disperse

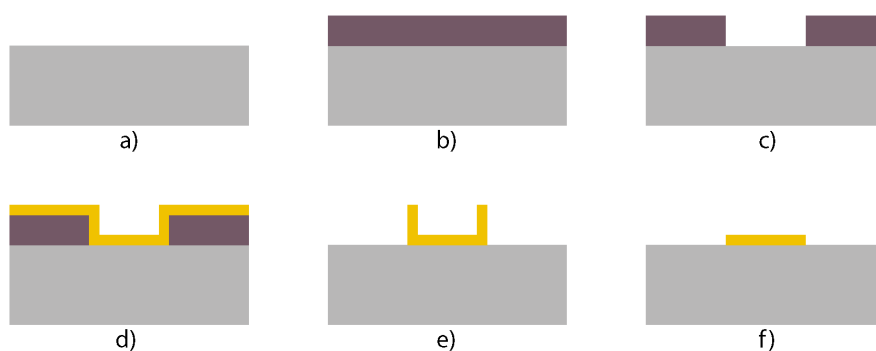


FIGURE 3.11: a) Clean Si substrate with SiO_2 layer. b) Spincoating of PMMA c) Exposition of PMMA to electron beam and development in IPA:water. d) Deposition of 3 nm Ti and 60 nm Au e) Lift-off process f) Clean structure without any rough edges.



FIGURE 3.12: Exfoliation of graphene using the scotch tape method [36].

the graphene/graphite flakes more evenly on its surface. The tape is placed over the sample and slowly stroked with low force over the area on which the graphene is supposed to be exfoliated for 10 minutes. When the time expires the tape is slowly removed from the sample surface and the sample is cleaned from any residual glue in acetone, IPA and demineralized water bath.

3.4 Atomic force microscopy

Atomic force microscopy (AFM) is based on the force interaction between surface atoms of the sample and a mechanical probe. AFM allows us to measure the height of a graphite flake and calculate the number of graphene monolayers, one layer should be 0.34 nm thick, however, the real height measured by AFM approaches to 1.5 nm [10] due to the contamination by adsorbant molecules (e.g. water). The most frequently used modes of AFM are the contact and semicontact.

Lennard–Jones potential [37] describes the force interaction, repulsive short range force and attractive van der Waals force, between the probe and the surface atoms:

$$w(r) = 4w_0 \left[\left(\frac{\sigma}{r} \right)^{12} - \left(\frac{\sigma}{r} \right)^6 \right] \quad (3.2)$$

r is the distance between the atoms, σ is a constant ($w(r=\sigma)=0$), w_0 is the minimum of potential in the point $r=1,12\sigma$. The corresponding interaction force between the atoms is [37]:

$$F(r) = -\frac{\partial w}{\partial r} = 24w_0 \left(2\frac{\sigma^{12}}{r^{13}} - \frac{\sigma^6}{r^7} \right) \quad (3.3)$$

Figure 3.13 shows a graph representing the coarse of the force function.

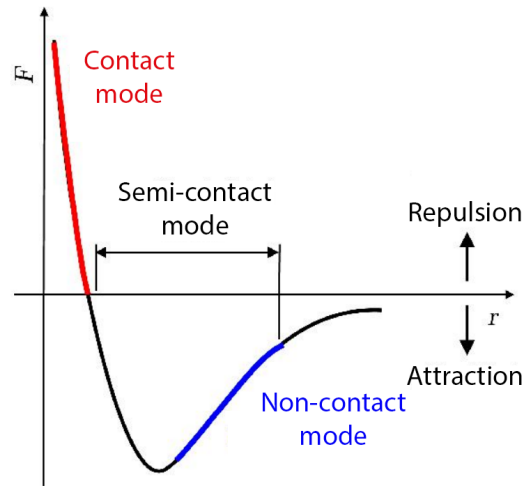


FIGURE 3.13: The coarse of the interaction force [37].

Each sample was measured in contact mode which works in the repulsive area of the force interaction. The probe deflection is measured using a laser beam reflected from the probe surface back to a PSPD (position sensitive photo detector). Using the contact mode, the surface height can be measured and also the friction using lateral force microscopy.

The height measured by AFM of the graphite/graphene layer can be affected by many factors, like for example by the contamination on the sample surface, the type of used AFM probe, set point of the AFM probe, or the relative humidity. All the measurements show that LFM has better contrast between the graphene flake and SiO_2 surface and the graphene layer. That is why LFM is used beside

the AFM during the measurements to recognize and identify the graphene flakes on top of the sample surface.

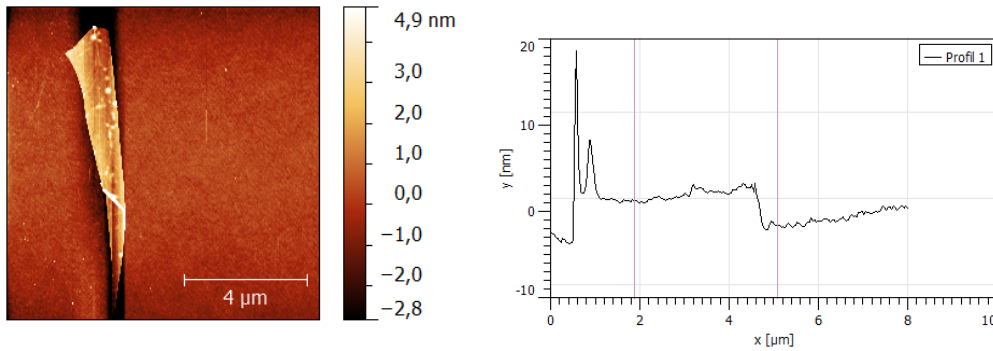


FIGURE 3.14: AFM image of a multilayer graphene flake with height profile (height between the 2 points marked by vertical lines is ≈ 2.5 nm).

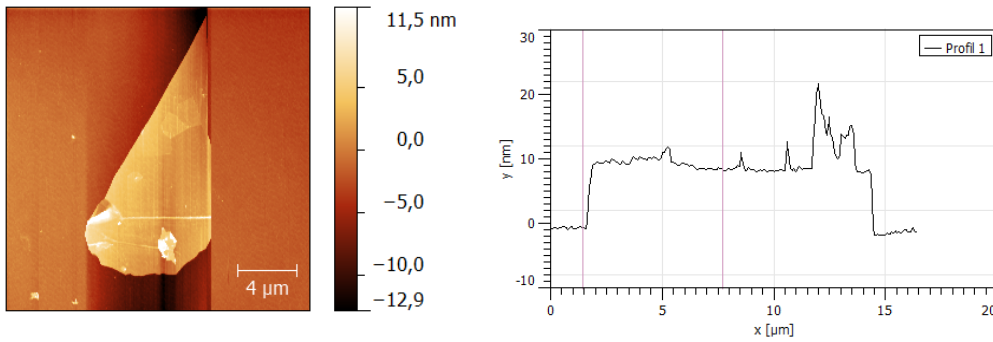


FIGURE 3.15: AFM image of a multilayer graphene flake with height profile (height between the 2 points marked by vertical lines is ≈ 8.7 nm).

The approximated height of the graphene flake shown in the Figure 3.14 is ≈ 2.5 nm and the different roughness of the SiO_2 .

Another sample measured by the AFM is shown in Figure 3.15 with the height approximately 8.7 nm with dimensions $8 \mu\text{m} \times 17 \mu\text{m}$, big enough to create a source and drain electrode and 4 other electrodes: 2 on each side for longitudinal and transversal transport properties measurements.

3.5 Raman spectroscopy

Raman spectroscopy is one of the methods used to identify graphene on the substrate surface, it can also distinguish between a monolayer and a multilayer graphene flake.

Raman scattering is an interaction between photon of the illumination source and the vibrational, rotational modes in atoms and molecules, in solid matter with the lattice vibration. Monochromatic light (usually from a laser) is scattered either elastically or inelastically.

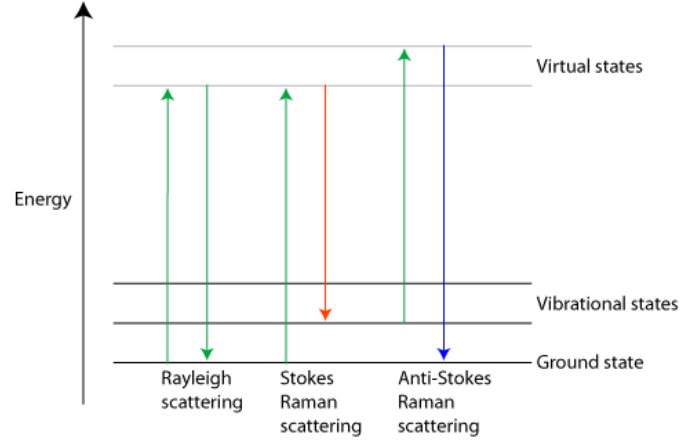


FIGURE 3.16: Energy–level diagram showing the states involved in Raman signal [38].

In the case of the inelastic scattering the energy of the incident photon and the emitted photon is different by quantum of energy. If the incident photon interacts with the crystal structure, part of his energy can be absorbed to create phonon and the emitted photon has a lower energy than before. This is called Stokes Raman scattering. Anti–Stokes Raman scattering is the opposite: the incident photon interacts with phonon, which transfers its energy to the scattered photon, so the emitted photon has higher energy than before. If the energy of the incident photon is:

$$E_i = \hbar\omega_i \quad (3.4)$$

then the photon emitted after the scattering has the energy:

$$E_f = \hbar\omega_f = \hbar\omega_i \pm \hbar\Omega \quad (3.5)$$

Ω is the frequency of the phonon and "–" is for Stokes and "+" for Anti–Stokes Raman scattering. Figure 3.16 shows each interaction of the light with the substrate and the changes of energy during this process. The signal from Raman

spectroscopy is the intensity of the light for each wavelength. Only the wavelengths which correspond to the energies of created/annihilated phonons and their multiples stand out from the spectra.

3.5.1 Raman spectroscopy of graphene

Each substance has its own unique Raman spectra, even graphene.

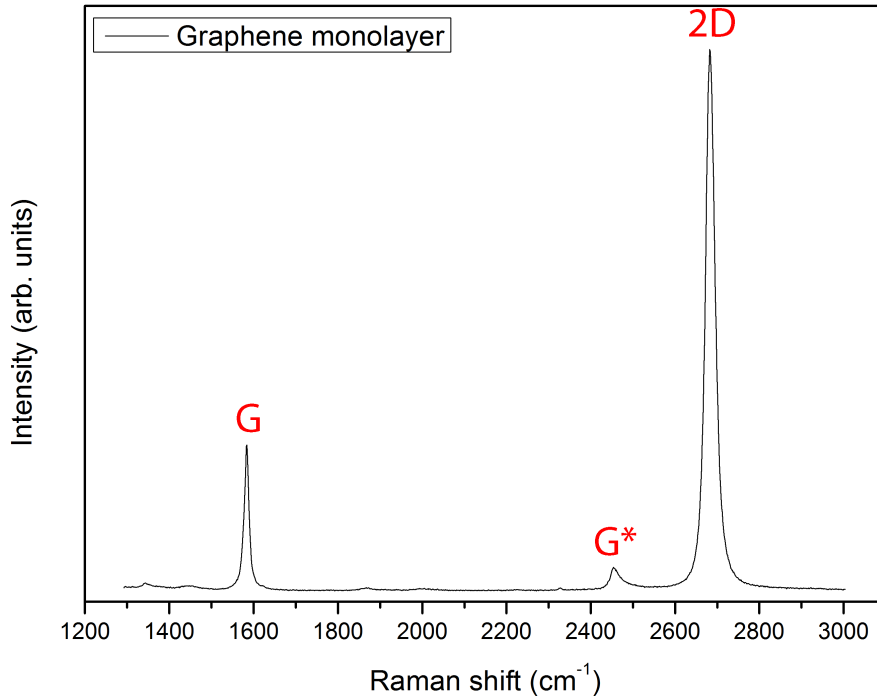


FIGURE 3.17: Raman spectra for excitation energy 2.41 eV of an exfoliated graphene on universal structures, with the positions of G, G* and 2D peaks.

Figure 3.17 shows the Raman spectrum for excitation energy 2.41 eV of an exfoliated graphene on top of SiO₂ with G peak at 1582 cm⁻¹, G* peak at 2450 cm⁻¹ and 2D peak at about 2700 cm⁻¹. The G band (peak) is associated with double degenerated (iTO and LO) phonon mode at the Brillouin center [39]. A second order process involving two iTO phonons near the K point is the origin of the 2D band (peak). If there are any defects found in the graphene layer, a D band peak at 1350 cm⁻¹ is present which originates from a second order process, involving one iTO phonon and one defect [39]. The intensity of the D band is proportional to the number of defects in the layer.

The shape, Raman shift and width of the 2D band (peak) determine the number of layers of graphene flake in Raman spectra. For a monolayer of graphene the

2D band exhibits a single Lorentzian feature with full width at half maximum of $\approx 24 \text{ cm}^{-1}$. The intensity of the 2D band is considerably large compared to the intensity of the G band [39].

Chapter 4

Experimental setup 2

4.1 Transport measurement

The measurement of transport properties is carried out as a measurement of resistance (2–point probe) or resistivity (4–point probe). With 2–point probe measurement the resistance of the contacts has to be taken into consideration, unlike the 4–point probe measurement which can neglect the resistance of the contacts.

4.1.1 2–point probe measurement

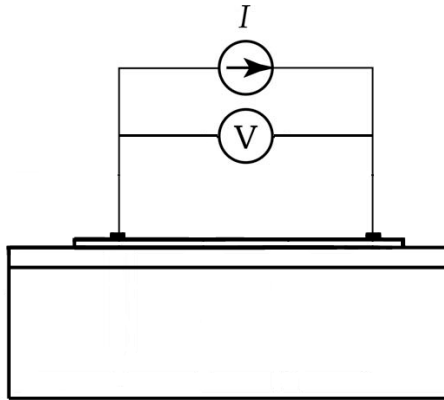


FIGURE 4.1: Scheme of a 2–point probe measurement using a current source and a voltmeter.

2– point probe method uses 2 contacts on a sample. The current source and voltmeter are directly connected to the contacts (Figure 4.1). The measured change of

potential between source and drain allows the calculation of resistance. Resistivity of a two dimensional material like graphene is then calculated as [40]:

$$\rho = R \frac{w}{l} \quad (4.1)$$

where w is the width and l the length of the sample. Conductivity is then calculated as:

$$\sigma = \frac{1}{\rho} = \frac{1}{R} \frac{l}{w} \quad (4.2)$$

4.1.2 4-point probe measurement

If there are 4 contacts on the sample the 4-point probe measurement method can be used. The sample dimensions have to be bigger than the distance between the electrodes. Figure 4.2 outlines the 2 used schemes for the 4-point probe measurement: either measuring the change of the potential between the source and drain, or placing one electrode between the source and drain and one behind the drain and measuring the change of potential.

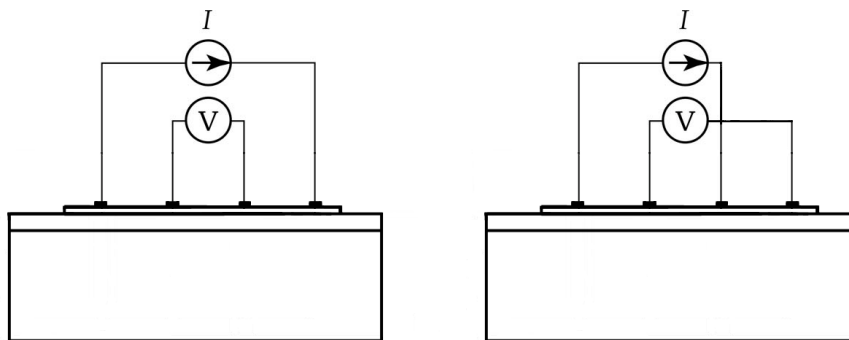


FIGURE 4.2: Scheme of a 4-point probe measurement with 2 variations using a current source and a voltmeter.

The resistivity of a two dimensional material is then calculated as:

$$\rho = R \frac{\pi}{\ln 2} \quad (4.3)$$

Since each sample has different shape a correction factor c has to be used.

$$\rho_r = c\rho \quad (4.4)$$

where ρ_r is the real resistivity of the sample and the correction factor c for rectangular structures is in the table 4.1 [41].

d/s	$a/d=1$	$a/d=2$	$a/d=3$	$a/d \geq 4$
1.0			0.9988	0.9994
1.25			0.9973	0.9974
1.5		0.9859	0.9929	0.9929
1.75		0.9826	0.9850	0.9850
2.0		0.9727	0.9737	0.9737
2.5		0.9413	0.9416	0.9416
3.0	0.8192	0.9000	0.9002	0.9002
4.0	0.7784	0.8061	0.9062	0.8062

TABLE 4.1: Correction factor c for various geometries as shown in Figure 4.3 [41].

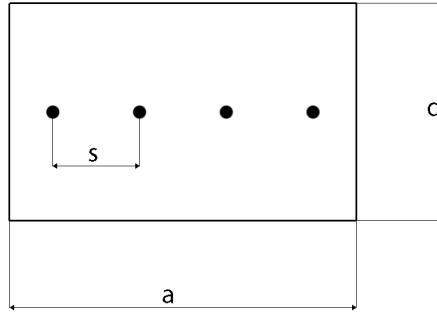


FIGURE 4.3: Geometry of the measurement, where d is the width, a is the length of the structure and s is the distance between the electrodes [41].

To overcome this problem the normal configuration is used in the first measurement of the resistivity, and in the second measurement the dual configuration is deployed, removing the statistical error of position and the geometrical error [42].

4.2 Setup of the transport properties measurement as a function of relative humidity

Figure 4.4 shows the scheme of the humidity chamber with automatic/manual regulation of relative humidity. The main parts of the humidity regulation system are: N_2 pressure gas bottle, flow regulator, electromagnetic valves, water reservoir, control sensor and humidity chamber. Manual mode allows to regulate the flow of the propulsion N_2 gas through or out of the water reservoir and achieve the required relative humidity by setting of a corresponding mixture of N_2 and H_2O vapors

in the chamber. Automatic mode allows to select the required value of relative humidity and the programmed PID controller (proportional–integral–derivative) automatically adjusts the flow rate and the gas type (N_2 , $H_2O_{(g)}$) to achieve the correct RH value.

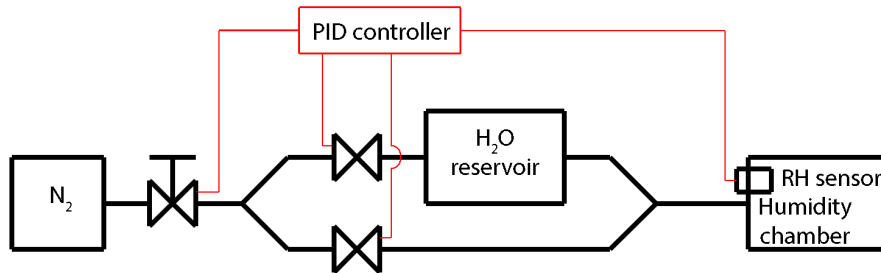


FIGURE 4.4: Scheme of the humidity chamber with regulation mechanism.

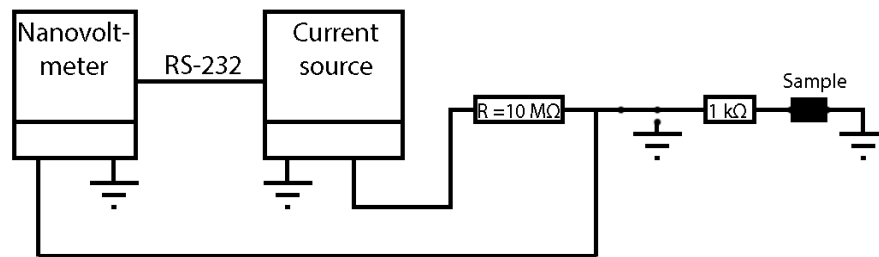


FIGURE 4.5: The configurations of 2-point probe measurement using a current source with nanovoltmeter.

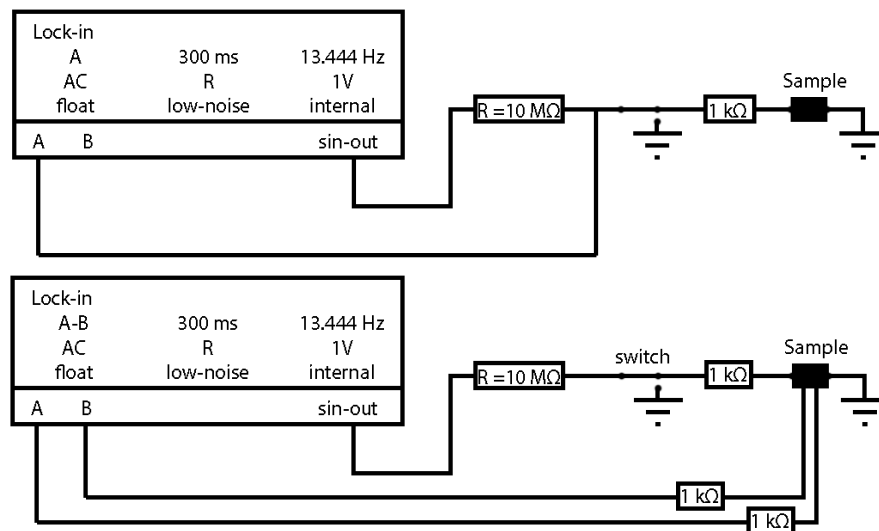


FIGURE 4.6: The 2 configurations of 2-point and 4-point probe measurement using a lock-in amplifier.

The transport properties of graphene inside the humidity chamber are measured using a current source (Keithley 2661AC) and a nanovoltmeter (2182A) (Fig. 4.5) or connected via the homebuilt protective apparatus shown in Figure 4.7 with

the lock-in amplifier (SR830 DSP Lock-in Amplifier, Stanford research systems) (Fig. 4.6), the homebuilt system prevents a discharge of static electricity, which would irreversibly damage the graphene sensor. Most of the measurements were performed by lock-in amplifier and only a few measurements were done by current source and nanovoltmeter (scheme on Fig. 4.5).

Figure 4.6 shows a schematic (wiring) diagram of so called two point method and diagram for the measurement of longitudinal part of resistivity. The lock-in amplifier has a sinus signal output and usually the following amplitude of 1 V at frequency 13.444 Hz was used (additional settings are shown in the scheme). The resistance of the circuit is determined mainly by the 10 M Ω resistor and the resulting current for the usual voltage was 100 nA. To protect the measuring devices a 1 k Ω resistor is placed behind the back contact.

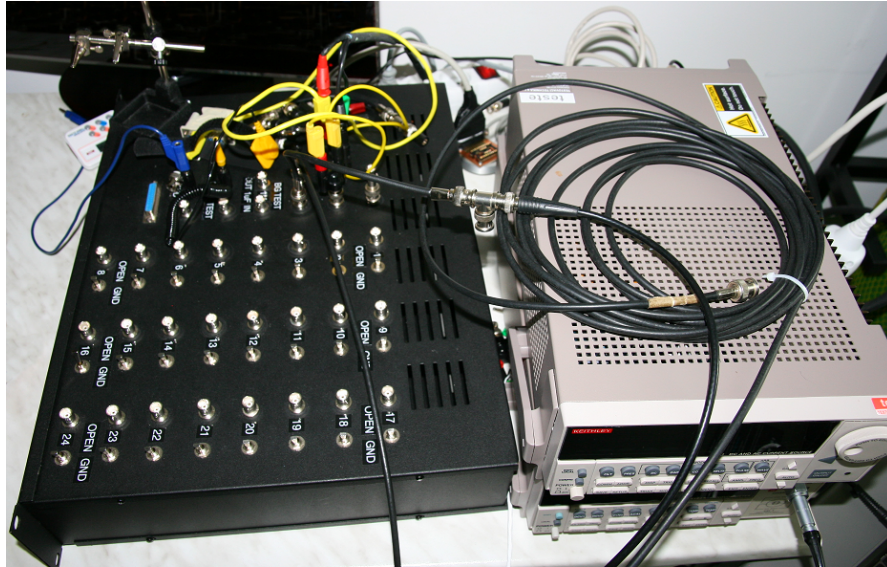


FIGURE 4.7: The homebuilt protective apparatus (on the left) and the current source (Keithley 2661AC) with the nanovoltmeter (2182A) (on the right).

The homebuilt protective apparatus (fig. 4.7) has a 25 pin cable with pins at the end to connect the sample as an input, and 25 separate outputs for each channel which can be separately grounded and opened, with 10 M Ω line for the source, 1 M Ω line for the gate voltage measurements, 1 k Ω line for testing of the setup and a grounding pin for grounding the user to avoid any damage caused by discharge of static electricity.

Both the lock-in amplifier and the current source with nanovoltmeter were controlled via GPIB by a computer with a program created in the programming environment of Labview.

Chapter 5

Results

5.1 2–point probe measurement of the graphene sensor response

5.1.1 Finger like electrodes

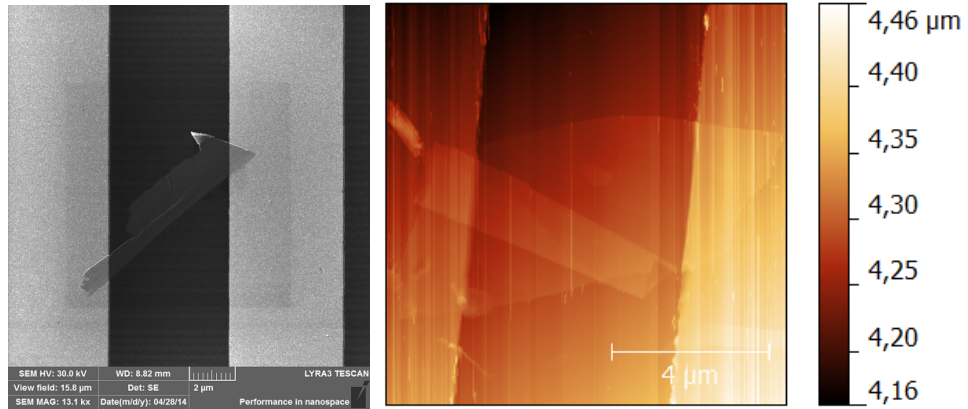


FIGURE 5.1: SEM and AFM image of the graphene flake on top of 2 finger like electrodes.

A graphene sensor (Fig. 5.1) was prepared on top of the interdigitated finger like electrodes, FIB (focused ion beam) was used to sputter away the unusable finger–like electrodes to make sure only one graphene layer was active during the measurement (Figure. 5.2 shows a small scheme of the process). The sample looks undamaged after the procedure, but the response of the sensor on the change of the relative humidity in time in Figure 5.3 exhibits a lot of noise. A small response

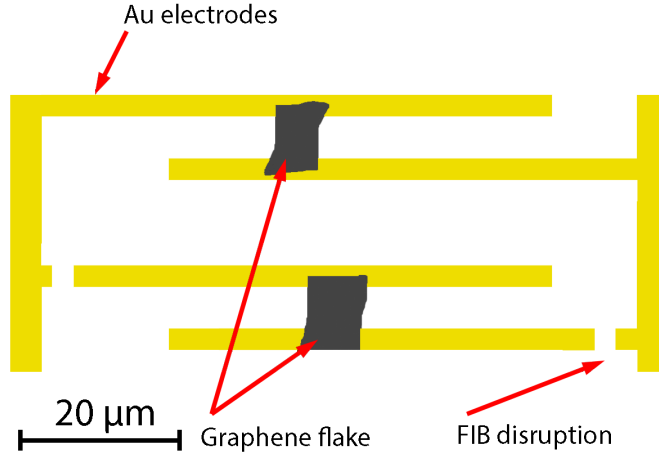


FIGURE 5.2: Scheme of 2 graphene flakes on top of gold electrodes, small part of the electrode was sputtered away to create a non conductive disruption.

of the sensor can be seen but it is very difficult to read. The change of the resistance is 0.1 % and sensitivity S is 0.1 % and the S_{RH} is 0.071 % for the change of RH from 10 % up to 70 %, sensitivity S is defined as:

$$S = \frac{R_2 - R_1}{R_1} \times 100\% \quad (5.1)$$

and S_{RH} related directly to the relative humidity RH:

$$S_{RH} = \frac{\frac{R_2 - R_1}{R_p}}{\frac{RH_2 - RH_1}{RH_p}} \times 100\% \quad (5.2)$$

where R_2 is the resistance response on the higher relative humidity RH_2 , R_1 is the resistance response on the lower relative humidity RH_1 , R_p and RH_p are the mean values of resistance and relative humidity. The sensor was probably damaged during the use of the FIB to sputter away the unwanted contacts and the surface of SiO_2 was doped with Gallium ions. Although it is damaged it shows a certain response on a change of relative humidity but for a stable measurement the signal has too much noise.

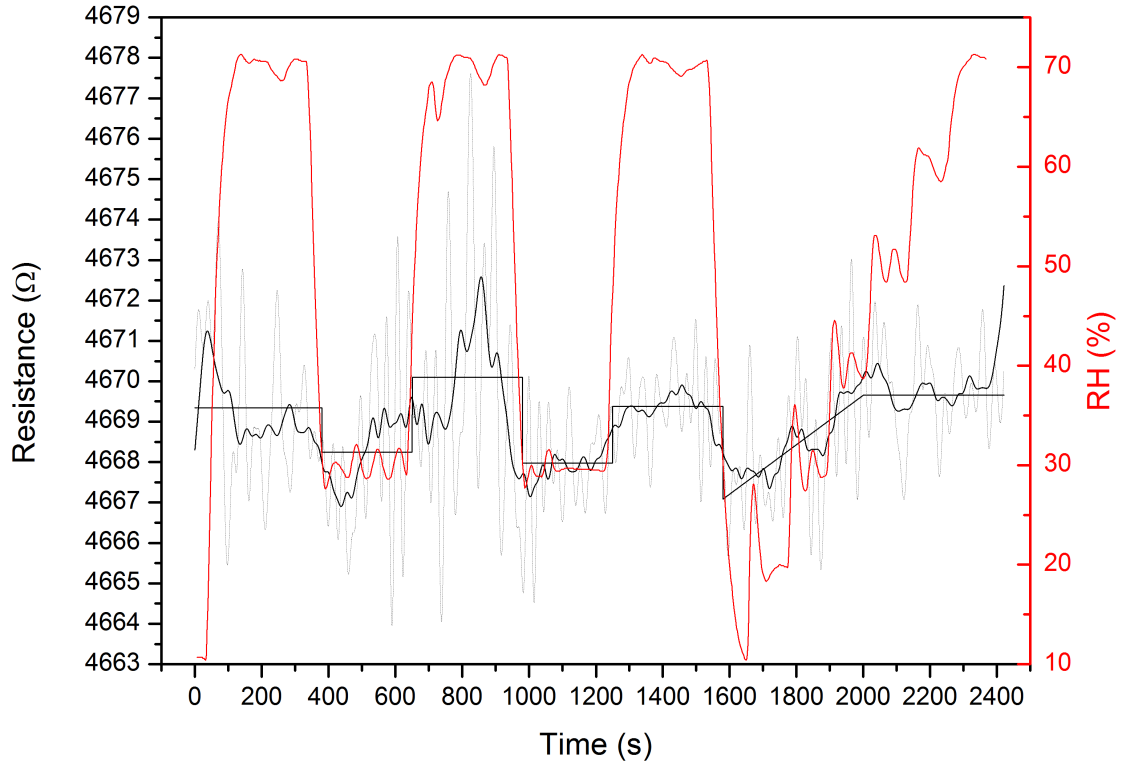


FIGURE 5.3: The response of the graphene sensor on a change of the relative humidity in time.

5.1.2 Universal electrodes

The sensor measurement in the Figure 5.4 shows a certain resistance responses on the change of relative humidity. In the first step change of relative humidity ($10 \rightarrow 70\%$), the average resistance decreases. Then, the resistance increases, although the RH is kept constant (70%), which is probably caused by the saturation by water vapors. The increase caused by saturation becomes milder when the RH goes down ($70 \rightarrow 30\%$) and is again kept constant (30%). In the second step, change of relative humidity ($10 \rightarrow 70\%$), the resistance increase was lower as can be expected- The following decrease of resistance at constant relative humidity (70%) was not expected and in agreement with the behavior observed previously, however in this case, the measurement is characterized by a strong noise.

The table 5.1 shows the sensitivity S and S_{RH} for the corresponding change of relative humidity RH. The sensitivity S shows a small decrease of sensitivity with smaller changes of relative humidity, but the S_{RH} which takes the RH into consideration clearly shows that the sensitivity is the highest around 70% and lowest for the change from 70% to 30% .

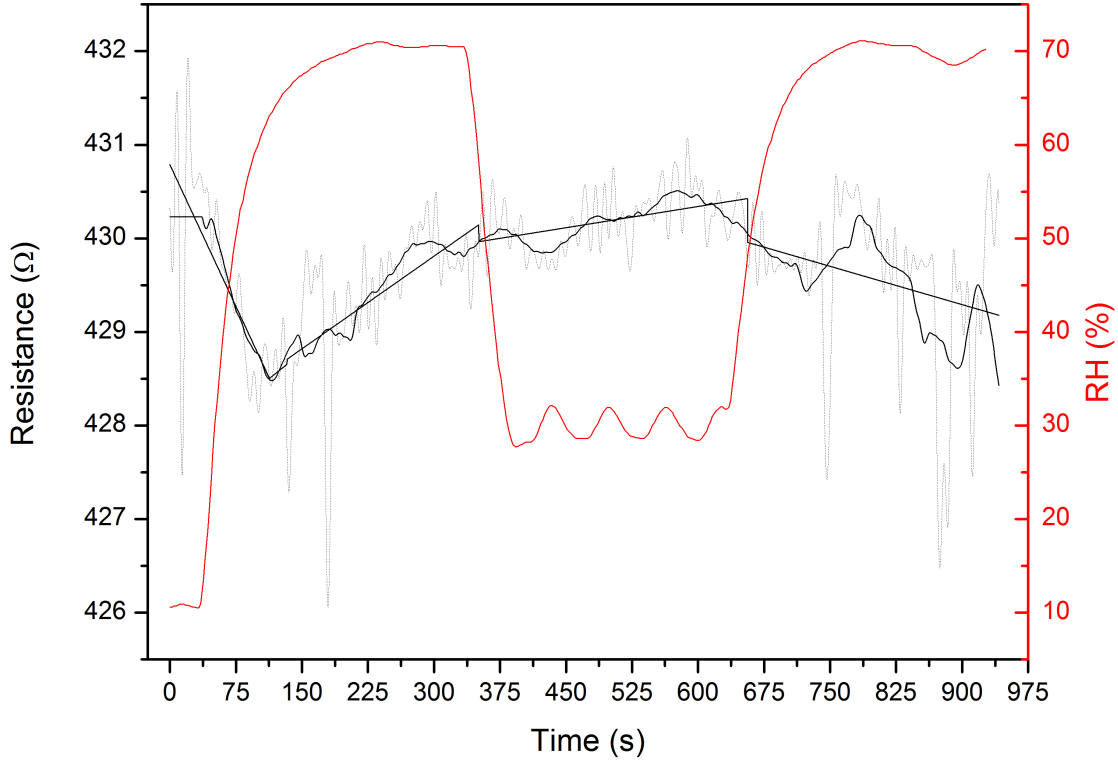


FIGURE 5.4: The dependence of the resistance and relative humidity in time of a graphene-based sensor on universal electrodes.

Change of RH (%)	S (%)	S_{RH} (%)
10–70	0,46	0,31
70–30	0,23	0,29
28–32	0,23	1,74
68–70	0,11	4,02

TABLE 5.1: The change of the relative humidity RH and corresponding sensitivity S and S_{RH}

5.1.3 Graphene flake with universal electrodes by applying a gate voltage

The graph in the Figure 5.6 is a resistance measurement in time depending on the change of the relative humidity of a graphene sensor shown in Figure 5.5. The graphene flake was $\approx 4.5 \mu\text{m}$ long and $\approx 0.8 \mu\text{m}$ wide in the middle. The back gate electrode was attached for field effect measurements. The measurement started at 10 % RH to desorb most of the water vapor from the graphene surface. The higher relative humidity increased the charge carrier concentration, since the resistance was lower. The graph at 70 % RH showed a linear decrease in resistance, which corresponded with the saturation of the surface by water vapors, but at 30 % the

resistance was constants, the small changes are caused by the RH fluctuations around the set relative humidity value.

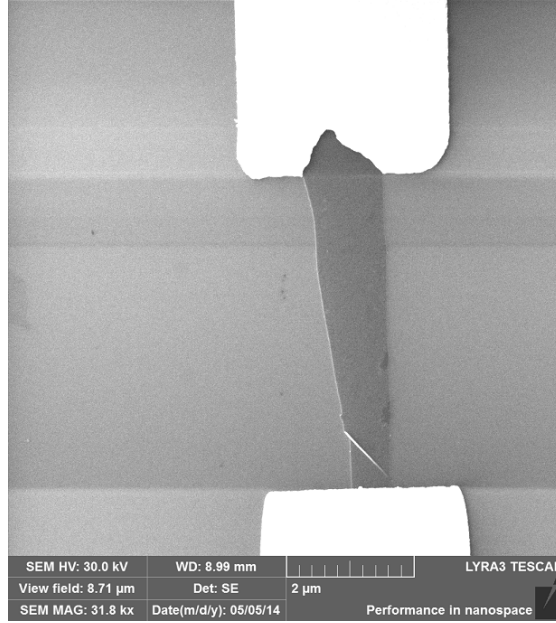


FIGURE 5.5: SEM image of a graphene sensor with 2 conductive contacts on universal structures.

Part 1			Part 2		
Change of RH (%)	S (%)	S_{RH} (%)	Change of RH (%)	S (%)	S_{RH} (%)
10–70	1,16	0,71	10–20	0,07	0,16
70–30	0,39	0,48	20–30	0,07	0,16
28–32	0,13	0,99	30–40	0,03	0,15
68–70	0,06	1,17	40–50	0,03	0,15
			50–60	0,06	0,36
			60–70	0,2	1,3

TABLE 5.2: The change of relative humidity RH and corresponding sensitivity S and S_{RH}

Table 5.2 and graph 5.7 show the sensitivity S and S_{RH} for different RH levels calculated from graph 5.6. The biggest $S_{RH} = 1,17\%$ was for RH around 70% and the lowest S_{RH} was in the range of 70–30% RH. The measurement of step like change of relative humidity from 10 to 70% at 10% RH steps, sensitivity was calculated and plotted as a function of relative humidity shown in Figure 5.7, S_{RH} increases exponentially from 50 to 70% RH. This exponential increase is contributed to the fact that at 50% RH the graphene surface approaches saturation from water vapor and the change of resistance is purely from the adsorption and desorption of water molecules.

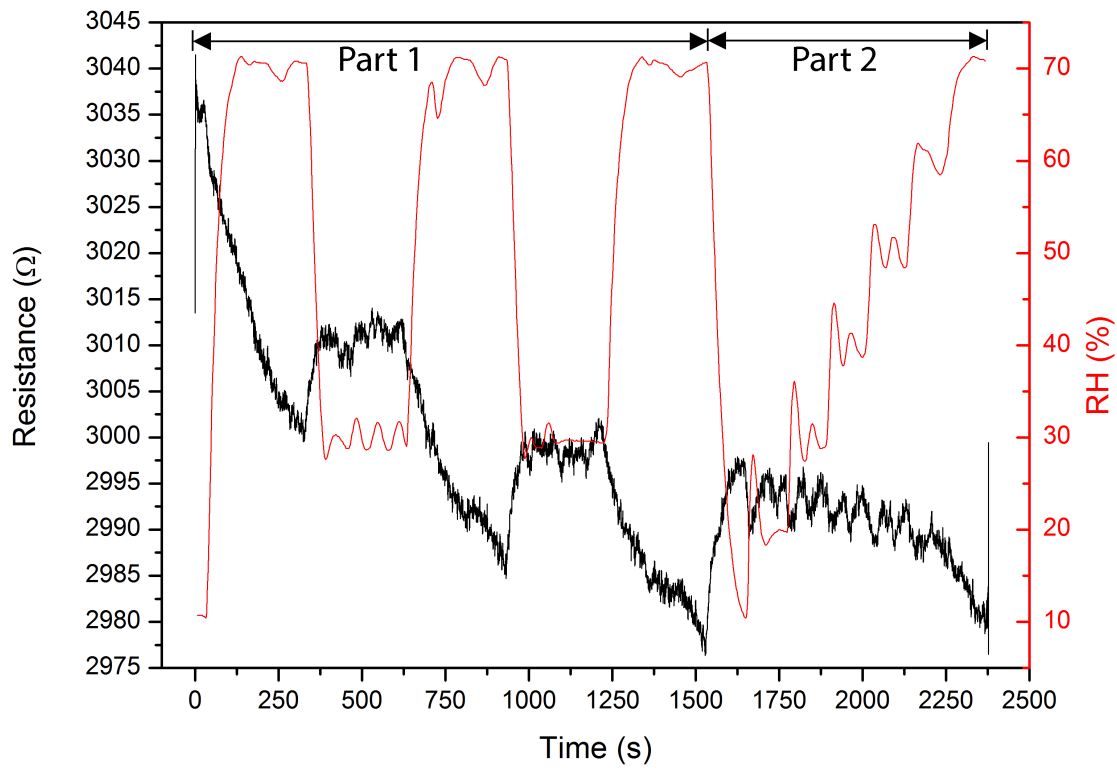


FIGURE 5.6: The dependence of the resistance and relative the humidity in time of a graphene-based sensor on universal electrodes.

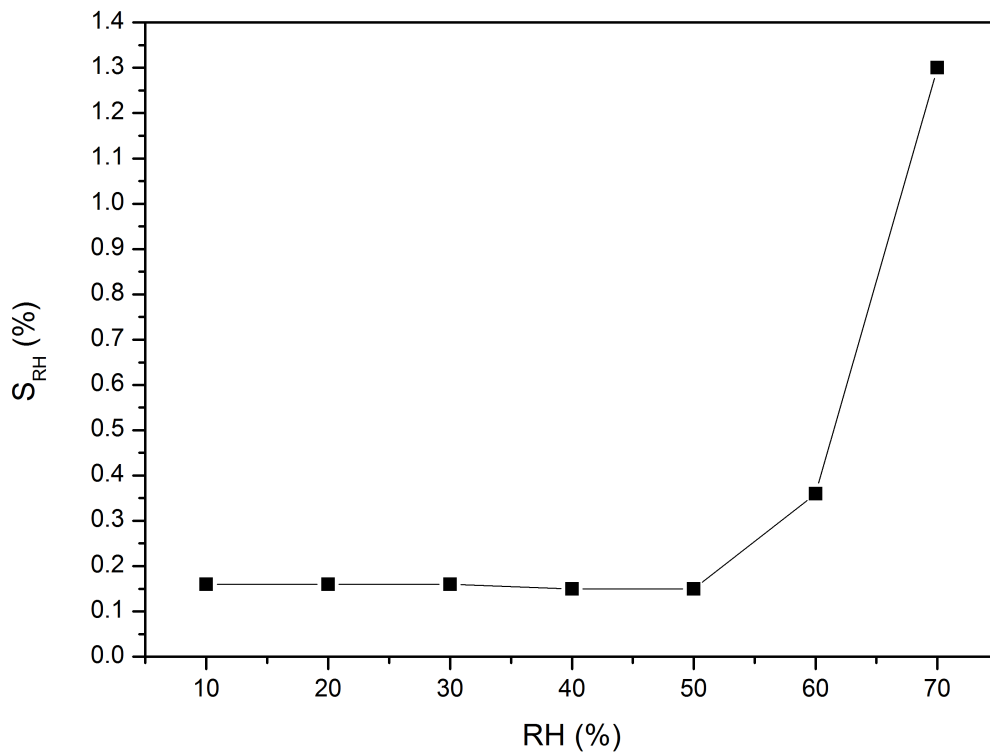


FIGURE 5.7: Sensitivity S_{RH} as a function of the relative humidity for the step-like changes in part 2 of the graph 5.6, from 10 to 70 % at 10 % RH steps..

5.1.4 Electric field effect measurement of the graphene sensor

Electric field effect measurement using a back gate electrode on the graphene sample was carried out before and after the measurement of resistance in time with changing relative humidity and back gate voltages set to -40 V, 0 V, 40 V, and the results can be seen in the Figure 5.8. The graph clearly shows the change of the graphene Dirac point from gate voltage ≈ 40 V to 18 V. The measurement of Dirac point indicate that measured exfoliated graphene flake was p-type, however, during the measurement of resistance response on relative humidity was doped by electrons.

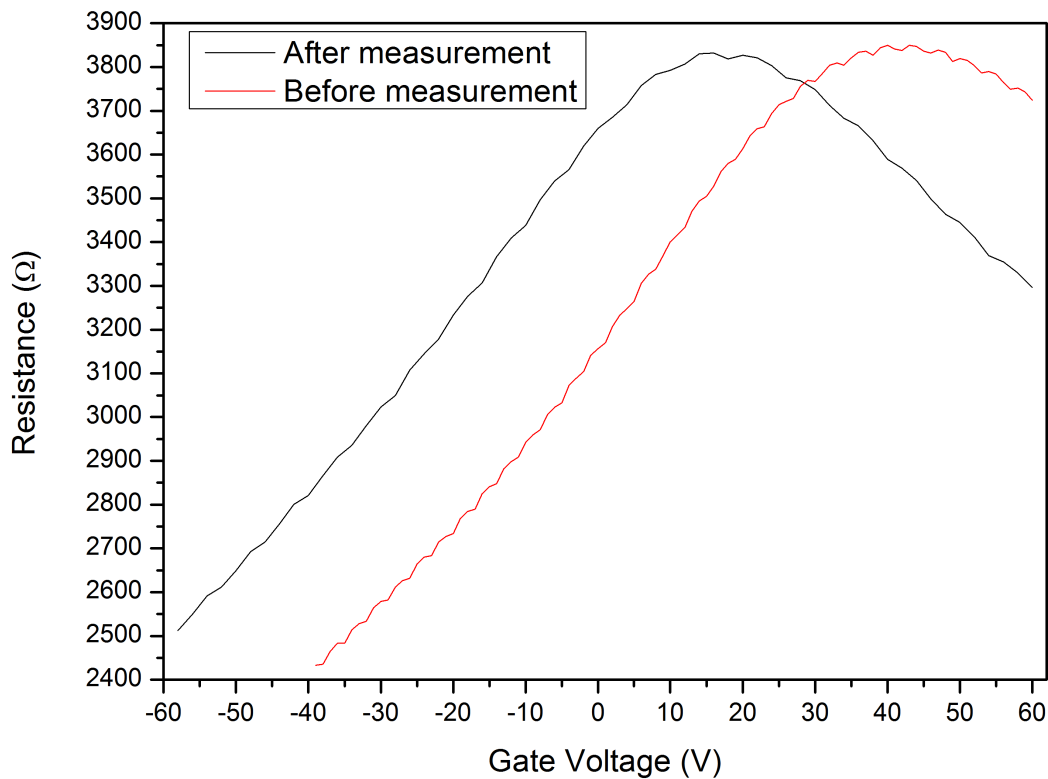


FIGURE 5.8: Electric field effect measurement

Figure 5.9 shows the different responses of the graphene sensor for each back gate voltage -40 V, 0 V and 40 V. Mostly, the resistance slightly increases/decreases with decrease/increase of the relative humidity for all the back gate voltages. This is very similar to the measurement presented in the chapters 5.1.2 and 5.1.3. However, there are quite big donations from this trend in time 500 – 1250 s at $BG = -40$ V (green curve) and in time 1250 – 2500 s at $BG = 0$ V (blue curve) in Figure 5.9, when a considerable increase of resistance occurred. This could be

caused by strong doping of graphene by electrons corresponding to the change of Dirac point position presented in Figure 5.8. It is difficult to explain the origin of this sudden n-type doping. Additionally also the increase of resistance in time for individual back gate voltages indicate the other slow doping by electrons.

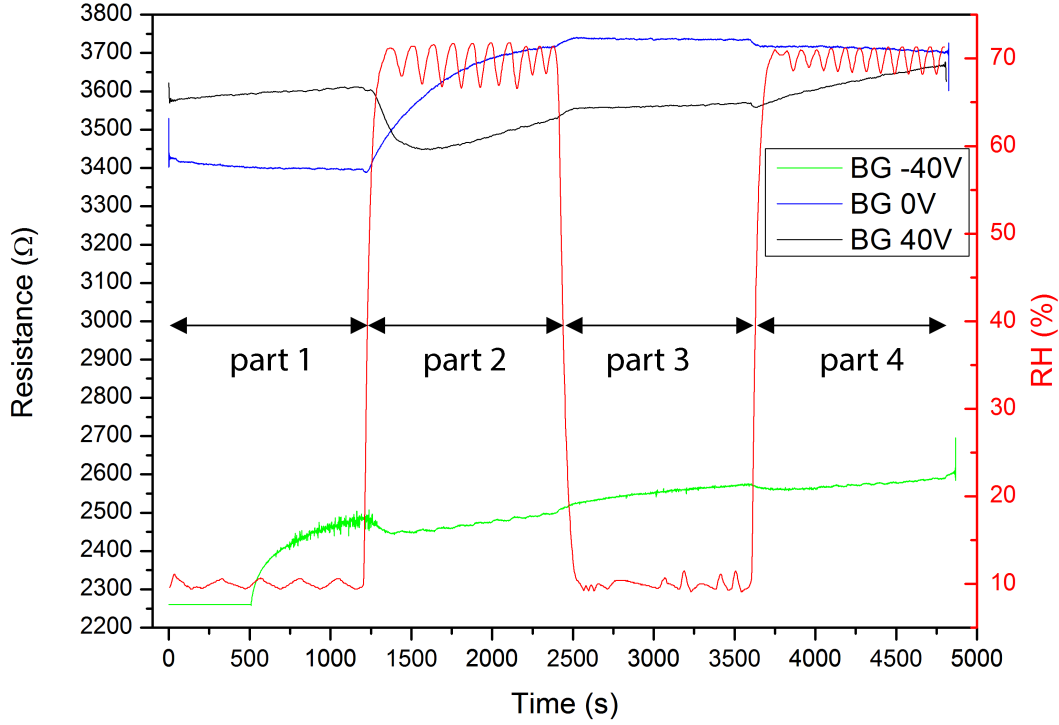


FIGURE 5.9: The dependance of the resistance and relative humidity in time of a graphene-based sensor with different back gate voltages -40 V, 0 V, and 40 V.

5.2 KPFM measurement of the graphene sensor

5.2.1 Using a lock-in amplifier

Kelvin probe force microscopy (KPFM) was used to measure the surface potential of the graphene flake (see Fig. 5.10) during the resistance in time measurement with changing of the relative humidity using a lock-in amplifier setup. There are numbered marks used to index events happening during the measurement in the Figure 5.11. Events like KPFM measurement, change of humidity or AFM measurement are highlighted. All the events are depicted in table 5.3, for example number 1 marks the start of an AFM semicontact measurement on an area of $5 \times 5 \mu\text{m}$ (detail of the graphene multilayer). There is a minor change of the resistance in the presence of the AFM tip near the graphene surface at $\approx 4\%$

RH (number 1). The KPFM measurement was performed with bias voltage 0 V at 4 % relative humidity, the KPFM image 5.12 shows an increase of surface potential near the area of higher number of graphene flake layers.

Ziegler, D. et. al., [43] observed the increase of the work function as a function of graphene layers number. However, they found out the change of work function between the SiO₂ substrate and first graphene layer of 150 meV, the second graphene layer added 100 meV the third layer 30 meV and the next layers had zero contribution, which quantitatively did not correspond to our result. Having regard to measurement errors and other influences, the KPFM probably showed only this information about the change of the work function with the number of layers.

The resistance of the graphene flake decreases with increasing number of graphene layers, because the current prefers areas with higher conductance (lower resistance). The linear increase of the resistance during the measurement around 5 % relative humidity was caused by the linear decrease of relative humidity to 3 %, but the increase around 50 % relative humidity was caused by the water vapor saturation of the graphene surface. Higher relative humidity caused higher resistance of the graphene sensor and showed that the graphene layer could be an n-type semiconductor.

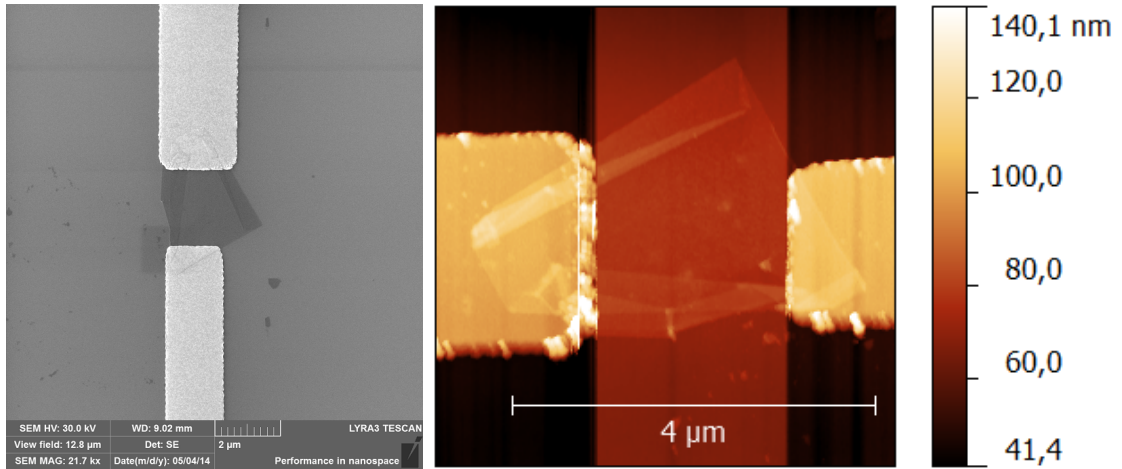


FIGURE 5.10: SEM and AFM image of the measured graphene multilayer.

The resistance measurement was carried out using a lock-in amplifier with a sine output signal, which causes fluctuations in the carrier concentrations and there is no gradient of surface potential between the electrodes.

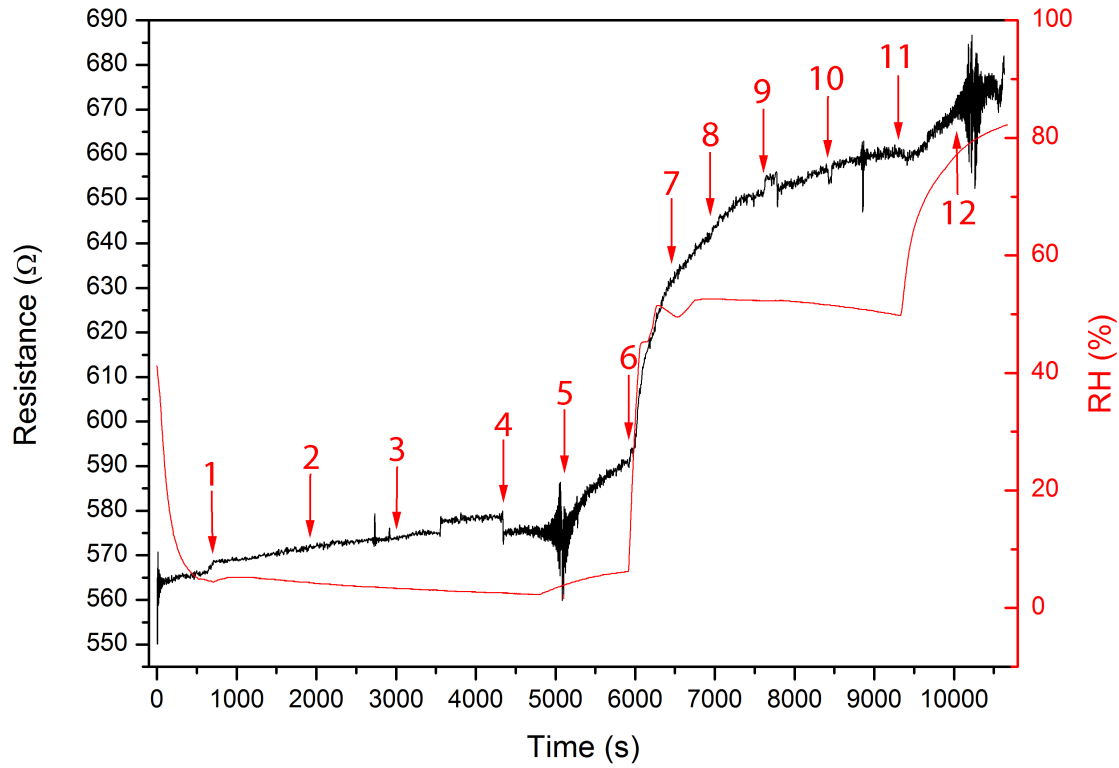


FIGURE 5.11: Change of resistance in time dependent on the relative humidity inside the humidity chamber with numbers marking AFM and KPFM measurement events.

Number	Event	Number	Event
1	AFM semicontact	7	KPFM at 0 V, 51,34 % RH
2	KPFM at 0 V, 4 % RH	8	KPFM at 10 V, 52,37 % RH
3	KPFM at 10 V, 3,42 % RH	9	KPFM at -10 V, 52,36 % RH
4	KPFM at -10 V, 2,55 % RH	10	KPFM at 0 V, 51,34 % RH
5	KPFM at 0 V, 3,49 % RH	11	change of RH up to 81 % RH
6	change of RH up to 51 %	12	KPFM at 0 V, 78,56 % RH

TABLE 5.3: The change of relative humidity RH with the sensitivity S and S_{RH}

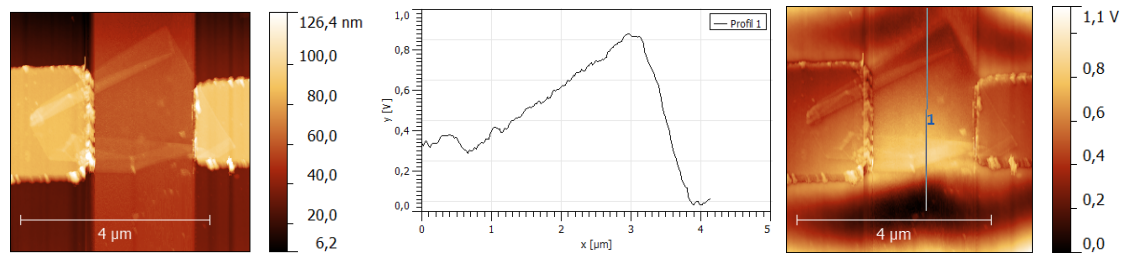


FIGURE 5.12: AFM and KPFM image of the measured graphene multilayer showing the distribution of potential on the surface at number 2 (RH=4 %).

5.2.2 Using a constant current source

The same graphene flake was used as in the measurement using universal electrodes with a back gate electrode, measured using Keithley 2661AC set as a constant current source. In a measurement like this, the authors usually suppose the visible linear surface potential change (KPFM) corresponding to voltage difference between grounded and voltage supplied electrode. In the case of this work such a behavior could not be observed due to small voltage difference (0.3 mV) corresponding to small constant current of 100 nA applied during the graphene flake measurement (resistance $\approx 3 \text{ k}\Omega$), to prevent the sample from destruction. Therefore, the changes of measured KPFM value should be contributed to different work functions of the gold, SiO_2 and graphene. However, without calibration of the tip work function, the KPFM gives information only about relative changes (KPFM measures the contact potential difference).

Graph 5.13 presents the result of resistance change in time with changing relative humidity at constant current. As in the subsection before the marks are used to index the events (in table 5.4) happening during the measurement, but the bias voltage was kept 0 V throughout all of the KPFM measurements. Scan with dimensions $8 \mu\text{m} \times 8 \mu\text{m}$ was used for KPFM measurements and a smaller scan was carried out to avoid any influence of the source and drain electrode with dimensions $3 \mu\text{m} \times 3 \mu\text{m}$.

Number	Event	Number	Event
1	approach with the tip	8	KPFM 48,14 % RH
2	KPFM 5,46 % RH	9	sub KPFM 48,05 % RH
3	sub KPFM 4,24 % RH	10	change of RH to 5 % RH
4	change of RH up to 35 %	11	KPFM 5,48 % RH
5	KPFM 34,94 % RH	12	sub KPFM 4 % RH
6	sub KPFM 35,01 % RH	13	KPFM 4,67 % RH
7	change of RH up to 50 %	14	sub KPFM 4,17 % RH

TABLE 5.4: The change of relative humidity RH with the sensitivity S and S_{RH}

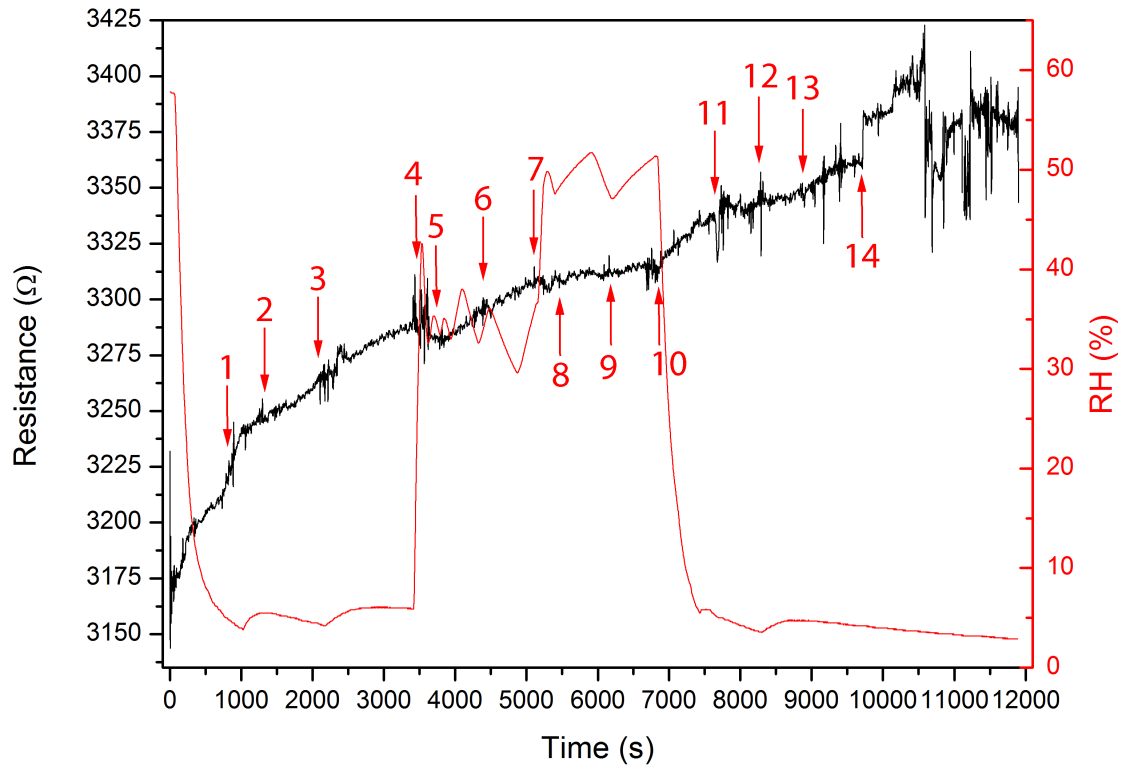


FIGURE 5.13: Change of resistance in time dependent on the relative humidity inside the humidity chamber with numbers marking AFM and KPFM measurements happening during the measurement.

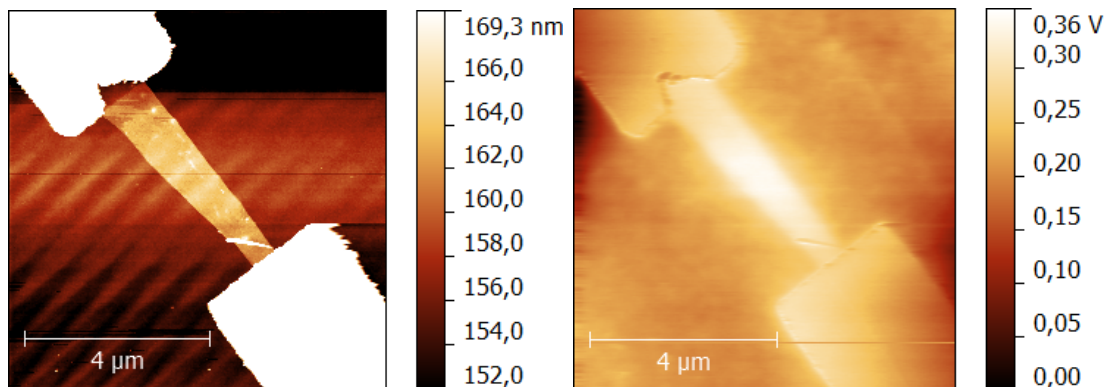


FIGURE 5.14: AFM and KPFM image of the measured graphene multilayer showing the distribution of potential on the surface at number 2 (RH = 5,46 %).

Chapter 6

Conclusion

This diploma thesis dealt with the fabrication and characterization of exfoliated graphene sensors of the relative humidity. On the bases of literature retrieval the following sensors were fabricated to meet the demands of this work.

1. Top graphene sensor on interdigitated finger–like electrodes
2. Bottom graphene sensor under the universal electrodes for 2–point and 4–point probe measurement.

The sensitivity of the sensors was estimated to a value of 0.1 %–1.3 % which was much smaller than the graphene oxide and CVD graphene published elsewhere. The 4–point probe measurement could not be realized due to multiple destruction of EBL structures. Moreover, the work studied the response of the sensor on the presence of AFM probe and KPFM measurement of the sensor during AC and DC current measurement, at different relative humidities. The leakage of the charge with higher relative humidity was not proved. Beneficial result also consisted in finding of the Dirac point of an exfoliated graphene in ambient conditions.

Bibliography

- [1] Schedin, F., Geim, a. K., Morozov, S. V., Hill, E. W., Blake, P., Katsnelson, M. I., and Novoselov, K. S. Detection of individual gas molecules adsorbed on graphene. *Nature materials*, 6 (9), **2007**, pp. 652–5.
- [2] Novoselov, K. S., Geim, A. K., Morozov, S. V., Jiang, D., Zhang, Y., Dubonos, S. V., Grigorieva, I. V., and Firsov, A. A. Electric field effect in atomically thin carbon films. *Science*, 306 (5696), **2004**, pp. 666–669.
- [3] Booth, T. J., Blake, P., Nair, R. R., Jiang, D., Hill, E. W., Bangert, U., Bleloch, A., Gass, M., Novoselov, K. S., Katsnelson, M. I., and Geim, a. K. Macroscopic graphene membranes and their extraordinary stiffness. *Nano letters*, 8 (8), **2008**, pp. 2442–6.
- [4] Ohno, Y., Maehashi, K., and Matsumoto, K. Chemical and biological sensing applications based on graphene field-effect transistors. *Biosensors & bioelectronics*, 26 (4), **2010**, pp. 1727–30.
- [5] Arash, B., Wang, Q., and Duan, W. H. Detection of gas atoms via vibration of graphenes. *Physics Letters A*, 375 (24), **2011**, pp. 2411–2415.
- [6] Yao, Y., Chen, X., Guo, H., and Wu, Z. Graphene oxide thin film coated quartz crystal microbalance for humidity detection. *Applied Surface Science*, 257 (17), **2011**, pp. 7778–7782.
- [7] Basu, S. and Bhattacharyya, P. Recent developments on graphene and graphene oxide based solid state gas sensors. *Sensors and Actuators B: Chemical*, 173, **2012**, pp. 1–21.
- [8] Yi, J., Lee, J. M., and Park, W. I. Vertically aligned ZnO nanorods and graphene hybrid architectures for high-sensitive flexible gas sensors. *Sensors and Actuators B: Chemical*, 155 (1), **2011**, pp. 264–269.

- [9] Novoselov, K. S., Jiang, D., Schedin, F., Booth, T. J., Khotkevich, V. V., Morozov, S. V., and Geim, a. K. Two-dimensional atomic crystals. *Proceedings of the National Academy of Sciences of the United States of America*, 102 (30), **2005**, pp. 10451–3.
- [10] Samsonau, S., Shvarkov, S., Meinerzhagen, F., a.D. Wieck, and a.M. Zaitsev. Growth of graphene-like films for NO₂ detection. *Sensors and Actuators B: Chemical*, 182 (2), **2013**, pp. 66–70.
- [11] Jaaniso, R., Kahro, T., Kozlova, J., Aarik, J., Aarik, L., Alles, H., Floren, A., Gerst, A., Kasikov, A., Niilisk, A., and Sammelselg, V. Temperature induced inversion of oxygen response in CVD graphene on SiO₂. *Sensors and Actuators B: Chemical*, 190, **2014**, pp. 1006–1013.
- [12] Wehling, T. O., Novoselov, K. S., Morozov, S. V., Vdovin, E. E., Katsnelson, M. I., Geim, a. K., and Lichtenstein, a. I. Molecular doping of graphene. *Nano letters*, 8 (1), **2008**, pp. 173–7.
- [13] Ko, G., Kim, H.-Y., Ahn, J., Park, Y.-M., Lee, K.-Y., and Kim, J. Graphene-based nitrogen dioxide gas sensors. *Current Applied Physics*, 10 (4), **2010**, pp. 1002–1004.
- [14] Dan, Y., Lu, Y., Kybert, N. J., Luo, Z., and Johnson, a. T. C. Intrinsic response of graphene vapor sensors. *Nano letters*, 9 (4), **2009**, pp. 1472–5.
- [15] Hwang, S., Lim, J., Park, H. G., Kim, W. K., Kim, D.-H., Song, I. S., Kim, J. H., Lee, S., Woo, D. H., and Chan Jun, S. Chemical vapor sensing properties of graphene based on geometrical evaluation. *Current Applied Physics*, 12 (4), **2012**, pp. 1017–1022.
- [16] Yoon, H. J., Jun, D. H., Yang, J. H., Zhou, Z., Yang, S. S., and Cheng, M. M.-C. Carbon dioxide gas sensor using a graphene sheet. *Sensors and Actuators B: Chemical*, 157 (1), **2011**, pp. 310–313.
- [17] Kang, X., Wang, J., Wu, H., Liu, J., Aksay, I. a., and Lin, Y. A graphene-based electrochemical sensor for sensitive detection of paracetamol. *Talanta*, 81 (3), **2010**, pp. 754–9.
- [18] Shao, Y., Wang, J., Wu, H., Liu, J., Aksay, I. A., and Lin, Y. Graphene Based Electrochemical Sensors and Biosensors: A Review. *Electroanalysis*, 22 (10), **2010**, pp. 1027–1036.

- [19] Pearce, R., Iakimov, T., Andersson, M., Hultman, L., Spetz, a. L., and Yakimova, R. Epitaxially grown graphene based gas sensors for ultra sensitive NO₂ detection. *Sensors and Actuators B: Chemical*, 155 (2), **2011**, pp. 451–455.
- [20] Massera, E., Ferrara, V. L. A., Miglietta, M., Polichetti, T., Nasti, I., and Francia, G. D. I. Gas sensors based on graphene. 29 (February), **2011**, pp. 39–41.
- [21] Arsat, R., Breedon, M., Shafiei, M., Spizziri, P., Gilje, S., Kaner, R., Kalantar-zadeh, K., and Wlodarski, W. Graphene-like nano-sheets for surface acoustic wave gas sensor applications. *Chemical Physics Letters*, 467 (4-6), **2009**, pp. 344–347.
- [22] Lu, G., Ocola, L. E., and Chen, J. Gas detection using low-temperature reduced graphene oxide sheets. *Applied Physics Letters*, 94 (8), **2009**, p. 083111.
- [23] Fowler, J. D., Allen, M. J., Tung, V. C., Yang, Y., Kaner, R. B., and Weiller, B. H. Practical chemical sensors from chemically derived graphene. *ACS nano*, 3 (2), **2009**, pp. 301–6.
- [24] Lu, G., Ocola, L. E., and Chen, J. Reduced graphene oxide for room-temperature gas sensors. *Nanotechnology*, 20 (44), **2009**, p. 445502.
- [25] Arsat, R., Breedon, M., Shafiei, M., Spizziri, P., Gilje, S., Kaner, R., Kalantar-zadeh, K., and Wlodarski, W. Graphene-like nano-sheets for surface acoustic wave gas sensor applications. *Chemical Physics Letters*, 467 (4-6), **2009**, pp. 344–347.
- [26] Fowler, J. D., Allen, M. J., Tung, V. C., Yang, Y., Kaner, R. B., and Weiller, B. H. Practical chemical sensors from chemically derived graphene. *ACS nano*, 3 (2), **2009**, pp. 301–6.
- [27] Chen, B., Liu, H., Li, X., Lu, C., Ding, Y., and Lu, B. Fabrication of a graphene field effect transistor array on microchannels for ethanol sensing. *Applied Surface Science*, 258 (6), **2012**, pp. 1971–1975.
- [28] Some, S., Xu, Y., Kim, Y., Yoon, Y., Qin, H., Kulkarni, A., Kim, T., and Lee, H. Highly sensitive and selective gas sensor using hydrophilic and hydrophobic graphenes. *Scientific reports*, 3, **2013**, p. 1868.

- [29] Bi, H., Yin, K., Xie, X., Ji, J., Wan, S., Sun, L., Terrones, M., and Dresselhaus, M. S. Ultrahigh humidity sensitivity of graphene oxide. *Scientific reports*, 3 (5 V), **2013**, p. 2714.
- [30] Zhao, C.-L., Qin, M., and Huang, Q.-A. Humidity sensing properties of the sensor based on graphene oxide films with different dispersion concentrations. *2011 IEEE SENSORS Proceedings*, , **2011**, pp. 129–132.
- [31] Leenaerts, O., Partoens, B., and Peeters, F. Adsorption of H₂O, NH₃, CO, NO₂, and NO on graphene: A first-principles study. *Physical Review B*, 77 (12), **2008**, p. 125416.
- [32] Geim, a. K. and Novoselov, K. S. The rise of graphene. *Nature materials*, 6 (3), **2007**, pp. 183–91.
- [33] MicroChem Corp, U., Newton. NANOTM PMMA and Copolymer. , **2008**.
- [34] Rai-Choudhury, E. P. Handbook of microlithography, micromachining, and microfabrication. *Bellingham: SPIE Optical Engineering Press*, 2, **1997**.
- [35] Tescan Orsay holding, C. r., Brno. Lyra 3 XMH. , **2014**.
- [36] HODGIN, R. C. Carbon one step closer to becoming viable alternative for silicon. , **2007**.
- [37] Bartošík, M. Aplikace AFM v oblasti nanotechnologií. *Brno: Vysoké učení technické v Brně, Fakulta strojního inženýrství*, , **102 p**, **2008**.
- [38] University of Cambridge, U. Raman scattering. , **2014**.
- [39] Malard, L., Pimenta, M., Dresselhaus, G., and Dresselhaus, M. Raman spectroscopy in graphene. *Physics Reports*, 473 (5-6), **2009**, pp. 51–87.
- [40] Klos, J. W., Shylau, a. a., Zozoulenko, I. V., Xu, H., and Heinzl, T. Transition from ballistic to diffusive behavior of graphene ribbons in the presence of warping and charged impurities. *Physical Review B*, 80 (24), **2009**, p. 245432.
- [41] Smits, F. M. Measurement of Sheet Resistivities with the Four-Point Probe. *The Bell system technical journal*, , **1957**, pp. 711–718.
- [42] Klarskov, M. B., Dam, H. F., Petersen, D. H., Hansen, T. M., Löwenborg, a., Booth, T. J., Schmidt, M. S., Lin, R., Nielsen, P. F., and Bø ggild, P. Fast

and direct measurements of the electrical properties of graphene using micro four-point probes. *Nanotechnology*, 22 (44), **2011**, p. 445702.

- [43] Ziegler, D., Gava, P., Güttinger, J., Molitor, F., Wirtz, L., Lazzeri, M., Saitta, a. M., Stemmer, a., Mauri, F., and Stampfer, C. Variations in the work function of doped single- and few-layer graphene assessed by Kelvin probe force microscopy and density functional theory. *Physical Review B*, 83 (23), **2011**, p. 235434.